UNIVERSIDADE ESTADUAL DE CAMPINAS
SISTEMA DE BIBLIOTECAS DA UNICAMP
REPOSITÓRIO DA PRODUÇÃO CIENTIFICA E INTELECTUAL DA UNICAMP

Versão do arquivo anexado / Version of attached file:

Versão do Editor / Published Version

Mais informações no site da editora / Further information on publisher's website:

https://aip.scitation.org/doi/10.1063/1.5088169

DOI: 10.1063/1.5088169

Direitos autorais / Publisher's copyright statement:

Brillouin optomechanics in nanophotonic structures (F)

View Online   Export Citation   CrossMark

Gustavo S. Wiederhecker,[1,2,a] (iD) Paulo Dainese,[2,3,4,b] (iD) and Thiago P. Mayer Alegre[1,2,c] (iD)

AFFILIATIONS

[1] Applied Physics Department, Gleb Wataghin Physics Institute, University of Campinas, Campinas 13083-859, SP, Brazil
[2] Photonics Research Center, University of Campinas, Campinas 13083-859, SP, Brazil
[3] Quantum Electronics Department, Gleb Wataghin Physics Institute, University of Campinas, Campinas 13083-859, SP, Brazil
[4] Corning Research & Development Corporation, One Science Drive, Corning, New York 14830, USA

Note: This article is part of the Special Topic "Optoacoustics—Advances in high-frequency optomechanics and Brillouin scattering" in APL Photonics.
[a] **Electronic mail:** gustavo@ifi.unicamp.br
[b] **Electronic mail:** dainese@ifi.unicamp.br
[c] **Electronic mail:** alegre@ifi.unicamp.br

ABSTRACT

The interaction between light and mesoscopic mechanical degrees of freedom has been investigated under various perspectives, from spectroscopy in condensed matter, optical tweezer particle trapping, and long-haul optical fiber communication system penalties to gravitational-wave detector noise. In the context of integrated photonics, two topics with dissimilar origins—cavity optomechanics and guided wave Brillouin scattering—are rooted in the manipulation and control of the energy exchange between trapped light and mechanical modes. In this tutorial, we explore the impact of optical and mechanical subwavelength confinement on the interaction among these waves, coined as Brillouin optomechanics. At this spatial scale, optical and mechanical fields are fully vectorial and the common intuition that more intense fields lead to stronger interaction may fail. Here, we provide a thorough discussion on how the two major physical effects responsible for the Brillouin interaction—photoelastic and moving-boundary effects—interplay to foster exciting possibilities in this field. In order to stimulate beginners into this growing research field, this tutorial is accompanied by all the discussed simulation material based on a widespread commercial finite-element solver.

I. INTRODUCTION

A. Context and brief history

When the phase of a propagating light field is disturbed by a spatially periodic modulation, the direction of light propagation is shifted as determined by momentum conservation.[1] If such a spatial modulation is also periodic in time, the Doppler effect takes place and energy conservation implies that the scattered light is frequency-shifted. As initially pictured by Léon Brillouin in his famous treatise *La diffraction de la lumière par des ultra-sons*,[2] mechanical waves can precisely induce such spatiotemporal gratings leading to the homonym scattering process: Brillouin scattering (BS). Motivated by Townes' pioneer experiments in nonlinear light-scattering,

Brillouin scattering gained importance in early experiments on optical fibers[3–5] and planar waveguides.[6] The enhanced interaction length brought by these waveguides fostered the investigation of Brillouin scattering,[6] although it is fair to say that it was within the optical fiber community that Brillouin scattering had the largest impact, either as a detrimental or gainful effect.

At high optical intensities, the interference pattern between the strong pump and the Brillouin back-scattered light—initially induced by thermal phonons—causes a back-action drive of the mechanical waves through electrostriction and radiation pressure forces.[7,8] Such feedback leads to the so-called backward Stimulated Brillouin Scattering (SBS) effect. In such a stimulated regime, Brillouin scattering can ultimately prevent high power signal

propagation through an optical fiber.[9] Despite the wider literature on the backward Brillouin scattering, a counterpart of it can also occur in the forward direction, first identified as GAWBS (Guided Acoustic Wave Brillouin Scattering) by Shelby *et al.*[10] in optical fibers experiments. The mechanical modes participating in those initial GAWBS observations were transverse standing waves with rather low resonant frequencies due to the large optical fiber cladding diameter (≈ 125 μm). Despite its weak thermal-noise origin, the phase noise induced by GAWBS was identified as a major source of noise in fiber-based quantum noise squeezing experiments.[10] These guided mechanical waves can also be stimulated by light through electrostriction forces and may lead to cross talk[11] and long range interaction[12] among short-pulses propagating in optical fibers.

The fundamentals and applications of SBS derived from these pioneer experiments impacted various research fields. For instance, the large and narrow band optical gain available through the Brillouin interaction has enabled efficient fiber-optic based slow and fast light,[13,14] nanosecond-long storage of optical pulses,[15] optical and radio-frequency (RF) tunable filters with unprecedented narrow band, extinction, and tunability.[16–19] Other technological breakthroughs enabled by the recent advances on Brillouin optomechanics are the generation of high-spectral purity RF sources,[20] distributed strain and temperature sensors,[21–25] high resolution spectrometers,[26,27] liquid-compatible sensors,[28,29] gyroscopes,[30] and narrow linewidth Brillouin lasers.[31–37]

For some of us, the love story with Brillouin started back in 2003 when selecting small-core photonic crystal fiber (PCF) samples for fiber-optical parametric amplification experiments at Bath University (UK). In the following years, in a joint effort between University of Campinas, FEMTO-ST in Besançon, and the Max Planck Research Group at Erlangen (now the Max Planck Institute for the Science of Light), we verified that the famous formula by Smith[38]—used for predicting the onset of SBS—consistently overestimated it for small-core PCFs.[39] Further investigation revealed that the strong optical and mechanical confinement in these fibers was responsible for the nonintuitive reduced overlap between optical and mechanical modes and, therefore, the overshoot of Smith's formula. At the time, similar predictions were made by Kobyakov and collaborators in weakly guiding optical fibers designed to suppress SBS.[40] PCFs not only triggered the possibility of controlling backward Brillouin scattering but also enabled the first observation of forward Brillouin scattering at gigahertz frequencies;[41] the mechanical waves were trapped at the 1.2 μm glass-air core interface, which drastically increased the GAWBS frequency and led to a broader wavevector range with near-zero mechanical group velocity, a property shared by the optical phonon branch in solids and inspired referring to GAWBS as Raman-like scattering.[41] Further work carried out by several groups using optical fibers[42–49] unraveled many remaining mysteries and potential applications of guided Brillouin scattering.

Parallel to these developments, the role of optical forces in photonic integrated cavities and waveguides was going through a revolution after a series of papers demonstrating the strong optomechanical interaction enabled by radiation pressure forces in high-index contrast devices.[50–58] In the last ten years, following the growth and availability of advanced top-down nanofabrication tools, a series of research breakthroughs occurred in this field within the

classical[59–61] and quantum realm.[62–67] The advancement of these integrated photonic structures also impacted backward Brillouin scattering, especially after the landmark demonstration of on-chip SBS by Pant *et al.*,[68] which sparked a convergence of the traditional waveguide-based Brillouin concepts with the cavity optomechanics ones. One clear outcome of this convergence was the prediction and subsequent demonstration of giant gain Brillouin scattering in a CMOS-compatible platform,[69–71] which culminated in the first generation of on-chip Brillouin lasers[20,35,36,72] and on-chip signal processing devices.[72,73] In the context of these recent demonstrations, it is harder to draw a line dividing the fields of Brillouin scattering in wave-guiding photonic structures and the field of cavity optomechanics. In light of this convergence, in this tutorial, we will use the term Brillouin optomechanics to encompass the whole spectra of experiments involving trapped light and mechanical waves.

B. Scope of this tutorial

There have been a series of reviews and tutorials published about the individual topics of Brillouin scattering and optomechanics in the recent years, with focus on optical fibers,[81] experimental progress,[82] integrated photonic applications,[83,84] phononics,[85] historical evolution,[86] surface modes,[87] electrostriction excitation,[88] and cavity optomechanics.[89] More recently, an extensive and detailed review article on current developments and future perspectives of light and sound interaction has been published by Safavi-Naeini *et al.*,[90] which brings together several aspects of electromechanical devices that share many similarities with optomechanical systems.[91–95] In this tutorial, we offer a complementary perspective aimed at providing a thorough discussion of the interaction between optical and mechanical modes in both waveguides and cavities as described by the coupled-mode theory. Since there is an extensive literature covering the derivations of the coupled-mode equations for both waveguides[79,96,97] and cavities,[79,98] and the fundamental[90] and technological[84] outcomes of this interaction, our focus will be on discussing the interplay between the two major mechanisms responsible for the Brillouin and optomechanical effects: the refractive index perturbations through the photoelastic effect[99] (PE) induced by the elastic strain and moving boundary (MB) effect caused by the mechanical mode distortion of the optical boundaries,[100] paying particular attention to highly confined optical and mechanical modes in nanophotonic structures. Doing so, we also cover the two major optical forces that enable driving mechanical modes with light, the electrostriction and radiation pressure forces, which are directly connected to the PE and MB refractive index perturbations.[96] To give an overview of the tutorial's scope, we show in Fig. 1 several structures where forward and backward Brillouin optomechanics have already been demonstrated, divided into fiber-based and integrated waveguides and axisymmetric cavities.

We organized this tutorial as follows: in Sec. II, we discuss the role of optical dispersion relation and momentum conservation (phase-matching) in both cavities and waveguides; general properties of the Brillouin optomechanical interaction are also discussed, including coupled-mode equations, definition of coupling rate and gain coefficient, and the structure of boundary and volume optomechanical overlap integrals. In Sec. III, we explore in detail Brillouin scattering in circular dielectric waveguides —specifically a silica glass rod suspended in air. In Sec. IV, we review in detail the
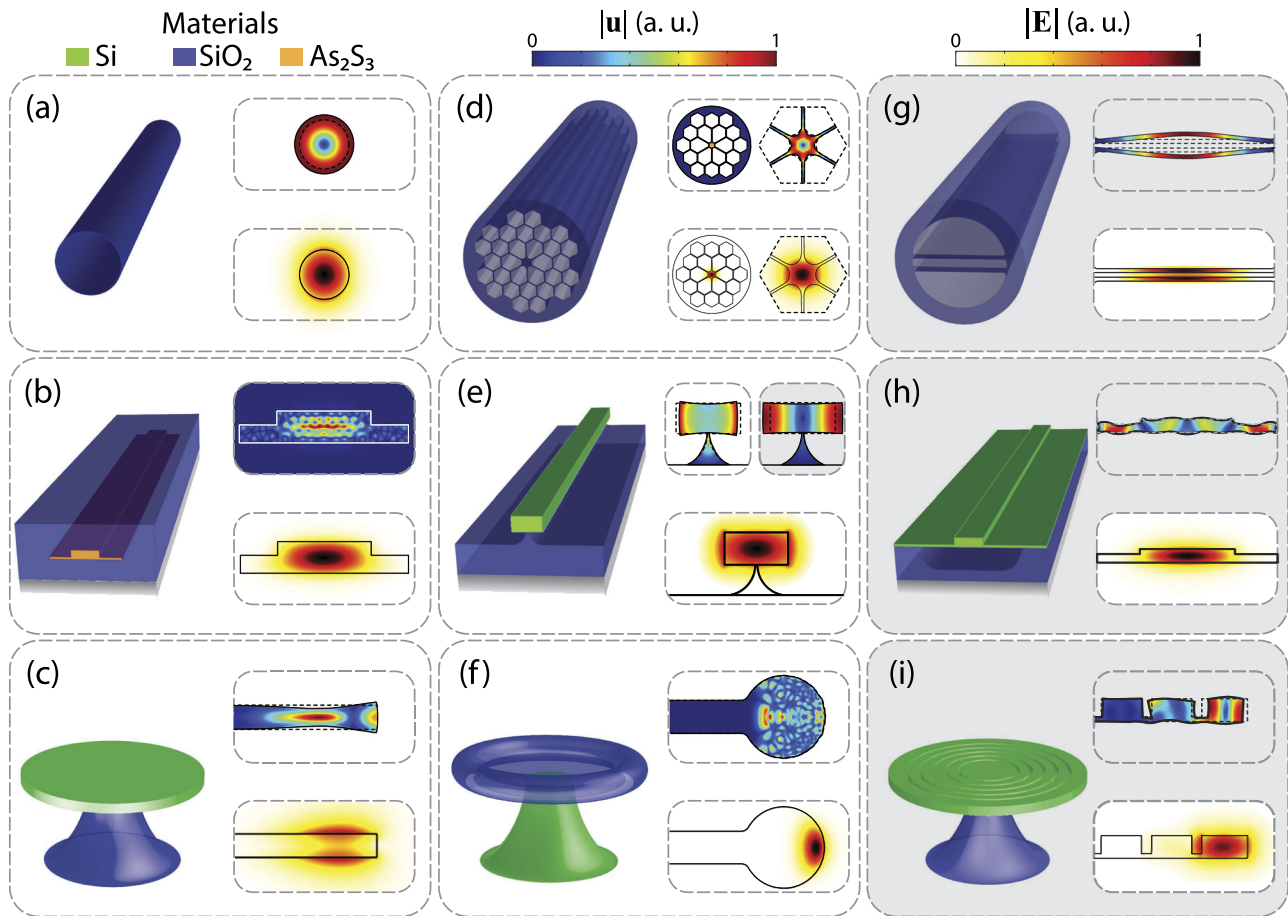
FIG. 1. Optical waveguide and cavity structures that have been commonly used to demonstrate Brillouin optomechanics based photonic devices. (a) Silica taper fiber,[74,75] (b) integrated As$_2$S$_3$ waveguide buried on SiO$_2$,[68] (c) simple Si disk,[76] (d) silica photonic crystal fiber,[39] (e) suspended silicon waveguide,[71] (f) toroidal silica cavity,[77] (g) dual-nanoweb silica fiber,[47] (h) suspended silicon waveguide membrane,[35] and (i) silicon bullseye optomechanical cavity.[78] For the typical dimensions, (a)–(f) present examples of mechanical modes for backward scattering, while (g)–(i) present examples of mechanical modes for forward scattering. In each panel, the top right inset shows the normalized total mechanical displacement ($|\mathbf{u}|$) and the bottom right inset shows the normalized absolute value of the electric field ($|\mathbf{E}|$). In order to compare the coupling strength between the optical and mechanical modes for each device, we extract g_0 [see Eq. (11)] from the simulations of the cavities and follow Ref. 79 to calculate $\tilde{g}_0$ [see Eq. (12)] using the same length for all circular cavities, equivalent to their perimeter ($L_{wg} = 2\pi \times 10\ \mu$m). The same approach is used to evaluate the gain coefficient (G_B/Q_m). The resulting mechanical frequency ($\Omega/2\pi$), effective coupling rate ($g_0/2\pi$), and the ratio between the gain and mechanical quality factors (G_B/Q_m) are (a) 6.0 GHz, 8.15 kHz, and 2.1 × 10^{-3} (W m)$^{-1}$; (b) 7.67 GHz, 110 kHz, and 1.3 (W m)$^{-1}$; (c) 16.7 GHz, 8.5 kHz, and 1.5 × 10^{-2} (W m)$^{-1}$; (d) 5.9 GHz, 0.65 kHz, and 2.2 × 10^{-5} (W m)$^{-1}$; (e) backward (left): 14.7 GHz, 17.5 kHz, and 5.3 × 10^{-2} (W m)$^{-1}$, forward (right): 9.2 GHz, 185 kHz, and 9.5 (W m)$^{-1}$; (f) 10.3 GHz, 8.4 kHz, and 2.1 × 10^{-3} (W m)$^{-1}$; (g) 6.5 MHz, 12.1 kHz, and 6.4 (W m)$^{-1}$; (h) 6.1 GHz, 20.0 kHz, and 1.2 × 10^{-1} (W m)$^{-1}$; and (i) 8.8 GHz, 149 kHz, and 5.7 (W m)$^{-1}$. In (e), forward and backward cases are presented as well as an example on the use of mechanical anisotropy for calculating modes and couplings in this geometry. A simulation file for each one of these devices is hosted on the data repository.[80]

optomechanical interaction in axisymmetric dielectric cavities, where the example of a silicon microdisk is explored and contrasted with other devices. Finally, general remarks and perspectives are outlined in the conclusions.

In order to fulfill the purpose of this tutorial, we also created an accompanying data repository[80] that includes most of the simulation files and processing scripts used in each of the figures. With the exception of some analytical tools, all the simulations were performed using the commercial finite-element solver COMSOL Multiphysics.

II. BASICS: DISPERSION RELATION, PHASE MATCHING, AND COUPLING

A. Dispersion relation and phase-matching

When optical and mechanical waves are localized inside a material, they can couple to each other and exchange energy through inelastic light-scattering. This is a two-way process, where either energy is transferred from the mechanical to the optical waves or the other way around. The inelastic scattering is due to the time-dependent refractive index grating induced by the mechanical wave.

In waveguides and cavities, mechanical and optical fields propagate in the eigenmodes of the structure obeying specific dispersion relations. If a pump laser at frequency ω_p is launched in an optical mode with the wavevector β_p, it propagates along the waveguide (z-direction) with a phase given by $\exp(-i\beta_p z + i\omega_p t)$ and may be scattered by a mechanical mode with frequency and wavevector (Ω, β_m) into a distinct optical mode (ω_s, β_s), provided the following energy and momentum relations are fulfilled:

$$\omega_s = \omega_p \pm \Omega, \tag{1a}$$

$$\beta_s(\omega_s) = \beta_p(\omega_p) \pm \beta_m(\Omega). \tag{1b}$$

The ± signs in these relations are due to Doppler effect and indicate that the scattered light may be blue-shifted (+ sign, anti-Stokes) or red-shifted (− sign, Stokes) from the pump; the wavenumbers $\beta_{p,s,m}$ can be positive- or negative-valued depending on the propagation direction. We illustrate such phase-matching conditions in Figs. 2(a) and 2(b). For example, in backward Brillouin scattering [$\beta_s(\omega_s) = -|\beta_s(\omega_s)|$], the phase-matched mechanical wavevector predicted by Eq. (1b) for the Stokes wave is $\beta_m(\Omega) = \beta_p(\omega_p) - \beta_s(\omega_p - \Omega) = |\beta_p(\omega_p)| + |\beta_s(\omega_p - \Omega)|$, which corresponds to a short-wavelength forward propagating ($\beta_m > 0$) mechanical mode, as shown in Fig. 2(a). In the case of forward Stokes scattering, the phase-matched mechanical mode is a long-wavelength forward propagating one. Therefore, in order to infer the phase-matched β_m, one needs to decide not only in which direction (forward or backward) the scattered light is being investigated but also whether the pump and scattered waves belong to the same transverse optical mode. Before we discuss some general aspects of the phase-matching in confined photonic structures, we explore how Brillouin scattering in axisymmetric optical cavities share similarities with their waveguide counterparts.

Within an axisymmetric optical cavity, the propagation phases for both optical and mechanical modes are in the form $\exp(-im\phi + i\omega t)$, where m is an integer and ϕ is the azimuthal angle. This phase dependence leads to a modified form of momentum conservation,

$$m_s(\omega_s) = m_p(\omega_p) \pm M(\Omega), \tag{2}$$

where $m(\omega)$ and $M(\Omega)$ represent the optical and mechanical dispersion relations for the cavity, respectively. Equation (2) is analogous to Eq. (1b), but the dispersion relation $\beta(\omega)$ is now attached to the azimuthal number frequency dependence $m(\omega)$; the azimuthal numbers $m_{p,s}$, M can also be positive-valued or negative-valued depending on the propagation direction, clockwise or counterclockwise. In addition, since the cavity resonance condition requires the azimuthal numbers m and M to be integers, the phase-matching points are discrete. An explicit connection between Eqs. (2) and (1b) can be drawn by mapping the propagation phase along the z-direction with the azimuthal coordinate, $z \rightarrow R\phi$, where R is the cavity radius; this implies that $\exp(-i\beta R\phi) \rightarrow \exp(-im\phi)$ and, therefore, $\beta = m/R$. This relation is quite useful and predicts the approximate values of the azimuthal numbers for an optical cavity mode with a given effective refractive index (n_{eff}) as $m \approx k_0 n_{eff} R$, where $k_0 = 2\pi/\lambda$ is the vacuum wavenumber at an optical wavelength λ.

In Fig. 2(c), we illustrate the most common forward and backward Brillouin scattering configurations studied in photonic structures, restricted to the Stokes scattering for simplicity. We generalize
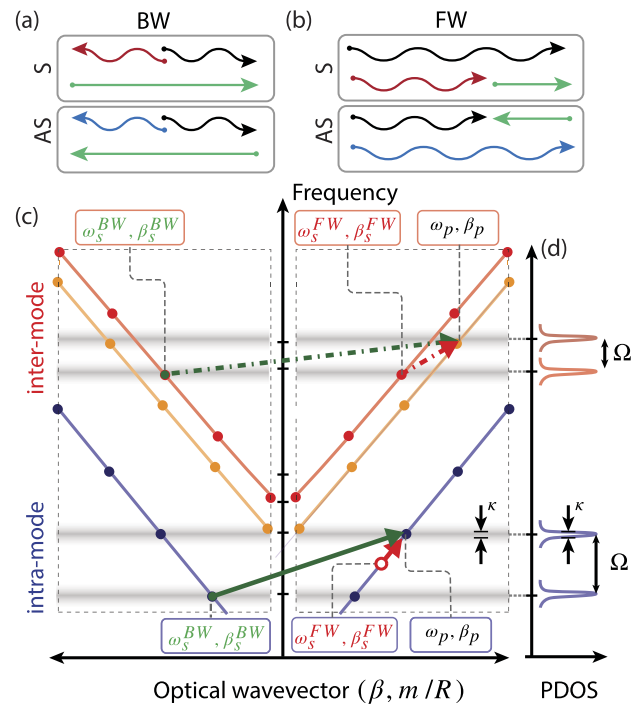
FIG. 2. Phase-matching in waveguide and axisymmetric cavity Brillouin scattering. Phase-matching schematic for (a) backward and (b) forward Brillouin scattering, where the black curved arrows represent the pump wave, and the curved red (blue) ones represent the Stokes (anti-Stokes) wave. (c) Optical dispersion diagram showing only the possible phase-matched Brillouin Stokes interactions. The solid curves represent dispersion branches for different optical modes, and the circles sampling the solid curves represent longitudinal resonances that are formed if the waveguide was wrapped into a cavity geometry; the shaded horizontal regions represent the linewidth of each optical mode resonance (κ). The arrows in the lower (upper) region correspond to the intramode (intermode) scattering. For the intramode set, an optical pump at (ω_p, β_p) is scattered to the same dispersion branch in the FW (BW) direction by forward propagating mechanical modes represented by the red arrow (green arrow). For the intermode set, an optical pump at (ω_p, β_p) is scattered to another dispersion branch in the FW (BW) direction by forward propagating mechanical modes represented by the red (green) dotted-dashed arrow. (d) Cavity resonance schematic representing the photonic density of states (PDOS) of the cavity modes. Notice that in the intramode FW case, the Stokes is detuned from the cavity mode (open symbol) effectively reducing the Stokes photons at the cavity mode.

this dispersion diagram schematic to represent the optical dispersion relation of both waveguides (solid lines) and cavities (discrete dots). We now distinguish between two scattering configurations: (1) intramodal and (2) intermodal scattering.

1. Intramodal scattering

In intramodal scattering, both pump and the scattered light propagate in the same transverse mode, in either of two directions, and therefore fall in the same dispersion relation branch; as illustrated in the lower part of Fig. 2(c). The backward case is the most common form of Brillouin scattering and can be easily observed in optical fibers.[3,5] In this configuration, the forward propagating pump at mode (ω_p, β_p) is back-scattered to (ω_s^{BW}, β_s^{BW}). Assuming

bidirectional[101] cavities or waveguides, i.e., $\beta_s(\omega) = -\beta_p(\omega)$ or $m_s(\omega) = -m_p(\omega)$, the phase-matching conditions [Eqs. (1b) and (2)] imply that

$$\beta_m^{\text{intra,BW}} = \mp[\beta_p(\omega_p) + \beta_s(\omega_p \pm \Omega)] \approx \mp 2\beta_p(\omega_p), \qquad (3a)$$

$$M^{\text{intra,BW}} = \mp[m_p(\omega_p) + m_s(\omega_p \pm \Omega)] \approx \mp 2m_p(\omega_p), \qquad (3b)$$

where we approximated $\beta_s(\omega_p \pm \Omega) \approx \beta_s(\omega_p)$ since the mechanical wave frequency is orders of magnitude lower than the optical frequency. This backward intramode process is represented by the solid green arrow in the lower part of Fig. 2(c). Albeit the waveguide phase-matching (β) can always be fulfilled, the cavity case (M) is far more restrictive: the frequency difference between the pump and scattered modes must match the mechanical frequency within the linewidth of the optical modes. In Fig. 3(a), we illustrate the mechanical dispersion relation of a waveguide (Ω, β_m) or axisymmetric cavity ($\Omega, M/R$)—the straight line represents the bulk-wave dispersion relation, and the hyperbolic curve with nonzero cutoff frequency represents the confined mechanical mode. The phase-matching condition for backward scattering given in Eq. (3) is represented by a dashed-gray line identified as BW. In either the waveguide or cavity geometry, the mechanical mode is a short-wavelength mode (large β_m), as indicated in Fig. 3(b). The symmetry of Eq. (3) with respect to Stokes and anti-Stokes scattering suggest that both are equally phase-matched, giving rise to two scattering peaks symmetrically positioned around the central pump frequency.

For intramodal backward scattering, a reasonably good estimate of the phase-matched mechanical frequency can be obtained by assuming a linear dispersion relation for both optical and mechanical modes, $\beta_p = k_0 n_{\text{eff}}$ and $\beta_m = \Omega/V_l$, with V_l being the longitudinal speed of sound. Inserting into Eq. (3), we obtain $\Omega \approx (4\pi/\lambda)n_{\text{eff}}V_l$. For a pump at λ = 1550 nm and a silica glass waveguide (n_{eff} = 1.45 and V_l = 5968 m/s), the phase-matched frequency is predicted to be $\Omega/2\pi$ = 11.16 GHz, which agrees pretty well with the experiments in pure-silica core fibers.[41] Similar predictions[76] can be made for axisymmetric optical cavities by employing the approximation $m_p \approx \beta_p R$. Tight confinement structures have multiple mechanical modes with dispersion relations that substantially deviate from

the linear dispersion relation of bulk longitudinal waves and, as a result, exhibit multiple phase-matching frequencies that differ from the above estimate. Further in this tutorial, several examples are explored to illustrate this point.

The case of forward intramodal scattering represents the usual interaction observed in the forward Brillouin scattering experiments[10,41,102] and many of the cavity optomechanics ones.[51,53,56] In this configuration, the forward propagating pump at mode (ω_p, β_p) is forward-scattered to ($\omega_s^{FW}, \beta_s^{FW}$) and the phase-matching conditions [Eqs. (1b) and (2)] result in

$$\beta_m^{\text{intra,FW}} = \mp[\beta_p(\omega_p) - \beta_s(\omega_p \pm \Omega)] \approx 0, \qquad (4a)$$

$$M^{\text{intra,FW}} = \mp[m_p(\omega_p) - m_s(\omega_p \pm \Omega)] \approx 0. \qquad (4b)$$

The phase-matching condition for forward intramodal scattering is represented in Fig. 3(a) as a vertical dashed line identified with FW. Notice that in the limit of (β_m, M) ≈ 0, forward intramodal scattering involves a mechanical mode at the cut-off frequency (i.e., at the waveguide transverse mechanical resonances). In either waveguide or cavity structures, these transverse resonances correspond to a uniform spatial phase along the propagation direction (z for waveguides or ϕ for axisymmetric cavities), as illustrated in Fig. 3(c). From the mechanical dispersion relation of Fig. 3(a), we note that the forward scattering phase-matching intercepts the mechanical modes very close to their cut-off frequencies. In contrast to the bulk mechanical dispersion [the straight solid line in Fig. 3(a)], these transverse resonances dispersion curves flatten out in the limit of null wavevector, resulting in very large mechanical phase velocities Ω/β_m. Such near-cutoff dispersion relation characteristics render forward intramodal Brillouin scattering analogous to Raman scattering in solids due to the flattened-out dispersion of the optical phonon branch.[41] Rigorously, the mechanical wavevector is not exactly null and can be estimated by exploring the fact that both scattered and pump waves have nearly the same frequency. Taylor expansion of the scattered optical wavevector around the pump frequency, i.e., $\beta_s \approx \beta_p + (\omega_s - \omega_p)\partial\beta/\partial\omega$, results in $\beta_m \approx \pm\Omega/v_g$ (v_g is the group velocity of the optical dispersion branch), which
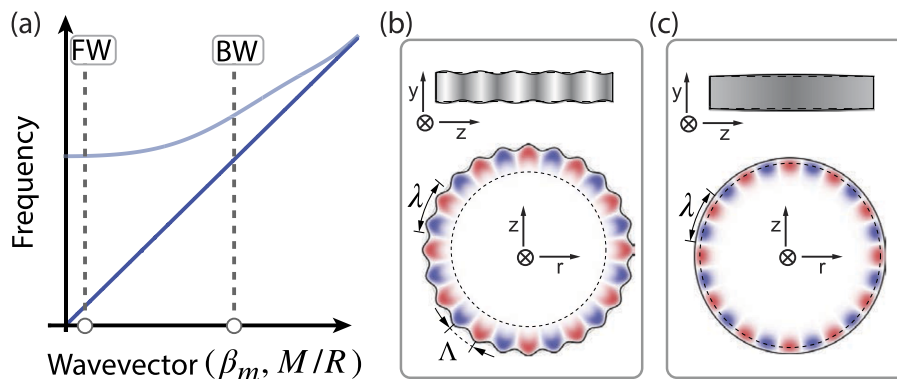
FIG. 3. (a) Schematic of the mechanical dispersion relation; the straight line represents the bulk-wave dispersion relation, and the hyperbolic curve with nonzero cutoff frequency represents the confined mechanical mode dispersion relation. Illustration of mechanical modes phase-matched for (b) backward and (c) forward Brillouin scattering in waveguides (top) and axisymmetric cavities (bottom). The colormaps in (b) and (c) represent the electric field, and blue (red) color represents the negative (positive) values; λ (Λ) is the optical (mechanical) wavelength. In (b), the curved boundary represents the short-wavelength mechanical wave, while in (c), the cavity expands radially with no azimuthal distortion.

compared to the pump wavevector is $\beta_m/\beta_p \approx \Omega/\omega_p \approx 10^{-5}$ (for $n_g = c/v_g \approx n_{\text{eff}}$). One can see that the Stokes and anti-Stokes scattered waves interact with very long wavelength mechanical modes ($\lambda_m \approx 20$ cm for a 1 GHz mode). Since either the mechanical attenuation length is shorter than such a wavelength or than the waveguide itself, the optical waves essentially interact with the same mechanical mode. For cavities, the existence of a finite lifetime ($1/\kappa$) allows for the pump and scattered light to couple to the same optical mode, although the number of intracavity photons will depend on the cavity photonics density of states (PDOS) at a given detuning [see Eq. (10)].[89]

2. Intermodal scattering

In intermodal scattering, the scattered light couples to a transverse optical mode distinct from the pump-wave mode, either in the forward or backward direction. In the backward configuration, represented by the dashed-dotted green arrow in the upper part of Fig. 2(c), the phase-matching conditions [Eq. (1b) and (2)] imply that

$$\beta_m^{\text{inter,BW}} = \mp[\beta_p(\omega_p) + \beta_s(\omega_p \pm \Omega)], \tag{5a}$$

$$M^{\text{inter,BW}} = \mp[m_p(\omega_p) + m_s(\omega_p \pm \Omega)]. \tag{5b}$$

On the other hand, the forward intermodal scattering, represented by the dashed-dotted red arrow in Fig. 2(c), contrasts with the forward intramodal case as the mechanical wavevector may be considerably larger, as given by the phase-matching condition,

$$\beta_m^{\text{inter,FW}} = \mp[\beta_s(\omega_p \pm \Omega) - \beta_p(\omega_p)], \tag{6a}$$

$$M^{\text{inter,FW}} = \mp[m_s(\omega_p \pm \Omega) - m_p(\omega_p)]. \tag{6b}$$

Note that the intermode phase-matching given by Eqs. (5) and (6) may also be applied between distinct nondegenerate polarizations of an given mode family, such as in between polarizations of fundamental modes in PCFs.[103] The mechanical wavevector imposed by the phase-matching is an important aspect of the mechanical mode engineering, and it is crucial in determining the mechanical group velocity and the attenuation length for a mode with a given dispersion relation $\beta_m(\Omega)$; it may also define whether mechanical bandgap guidance is feasible.[104] Therefore, although we cannot make any further assumption about the relation between β_s and β_p in Eqs. (5) and (6), it is instructive to analyze and compare the limiting cases of BW and FW scattering on a dielectric waveguide based on the optical total internal reflection. In this case, the guided optical wavevector is limited to the range $\beta_{\text{clad}} < \beta < \beta_{\text{core}}$, where $\beta_{\text{clad}} = k_0 n_{\text{clad}}$ ($\beta_{\text{core}} = k_0 n_{\text{core}}$) is the cladding (core) material wavenumber; n_j is their respective refractive indices. For BW intermodal scattering, the *shortest* wavevector mismatch is given by $\beta_m^{\text{inter,BW}} \approx \mp(\beta_{\text{core}} + \beta_{\text{clad}})$. In a low contrast silica-on-air structure, such an intermodal wavevector differs slightly from the intramodal case [Eq. (3)], $(\beta_m^{\text{inter,BW}}/\beta_m^{\text{intra,BW}})_{\text{SiO}_2} \approx (1.45 + 1)/(2 \times 1.45) \approx 0.85$. However, in higher index-contrast waveguides such as silicon-on-air structures, intermodal scattering may offer a larger range of possible mechanical wavevectors, $(\beta_m^{\text{inter,BW}}/\beta_m^{\text{intra,BW}})_{\text{Si}} \approx 0.65$. Despite such possibility of probing a larger portion of the mechanical dispersion relation, BW intermodal scattering has not been deeply investigated in waveguide Brillouin experiments. Nevertheless, such a possibility of phase-matching to different transverse modes was a key factor enabling the first observation of Brillouin scattering in silica

microsphere cavities.[105] For comparison, the *largest* wavevector mismatch for FW intermodal scattering can be estimated as $\beta_m^{\text{inter,FW}} \approx \mp(\beta_{\text{core}} - \beta_{\text{clad}})$. In a silicon-on-air structure, it could result in a larger forward intermodal wavevector, $(\beta_m^{\text{inter,FW}}/\beta_m^{\text{inter,BW}}) = (3.45 - 1)/(3.45 + 1) = 0.55$. In practice, this ratio will be smaller due to modal guidance constraints, but it shows that intermodal forward scattering can also involve short-wavelength (large wavevector) propagating mechanical modes. At such large wavevectors, the mechanical wave bounces from the guiding structure boundaries at an angle, which may drastically change the mode behavior; for instance, mechanical total internal reflection and phononic bandgaps may be completely modified at blazing incidence.

As a historical note of forward intermodal scattering, it was first reported by Engan *et al.* in a two-mode optical fiber with the mechanical wave driven by a piezoactuator,[106] and a couple of years later, it was observed as stimulated scattering by Russell *et al.*[107] Recently, it has been the configuration of choice in important Brillouin experiments in microphotonic structures.[35,108,109] Within optical microcavities, such short-wavelength mechanical modes can also be explored to ensure that the scattered light is resonant with one of the cavity modes, a technique that has been used[35,72,108] to demonstrate Brillouin lasing in integrated photonic cavities.

B. Photoelasticity and moving boundary perturbations: Electrostriction and radiation pressure forces

Although the phase-matching conditions discussed so far are necessary to ensure efficient optomechanical energy transfer, they are not sufficient. The optical and mechanical modes must have a reasonable spatial overlap and effectively perceive each other through some underlying physical effect. In the PE effect, the dielectric permittivity is disturbed by the elastic strain,[1,8] while in the MB, geometrical distortions of the optical boundary induced by the mechanical wave perturb the guided mode effective refractive index.[100] The latter was first noticed as a secondary contribution in thin-film scattering experiments[6] but has been demonstrated to be critical in subwavelength scale photonic structures.[62,69,74,88,96] These two effects together are responsible for light scattering by mechanical waves in the various configurations described in Sec. II A. It is worth noting that although photoelasticity and moving boundary perturbation are the main forward effects responsible for the Brillouin optomechanical interaction considered here, other coupling mechanisms exist, such as thermomechanical[8] and magnetoelastic[110] coupling.

Within optical waveguides, the Brillouin optomechanical interaction is described through the spatiotemporal evolution of slowly varying optical and mechanical field amplitudes along the propagation direction, while in optical cavities, the time evolution of the slowly varying fields describes the interaction. One may follow a few distinct approaches to derive such coupled equations. A classical one starts from Maxwell's and elastodynamics wave equations with a forward effect, describing how optical fields are perturbed by the mechanical waves (such as photoelastic and moving boundary effects), and a backward effect representing the electromagnetic forces driving the mechanical modes (such as electrostriction and radiation pressure). This path has been explored for both waveguides[96,111] and cavities.[64] Another common approach to derive the

coupled-mode equations, which only relies on energy conservation, starts directly from the classical or quantum mechanical Hamiltonian for waveguides[71,90,112–116] or cavities[89,90,117] where the photoelastic and moving boundary effects are directly incorporated in the Hamiltonian. The cavity and waveguide descriptions may also be directly linked to each other by employing a mean-field approach that averages out the cavity field dependence along the round-trip path—similar to the derivation of the Lugiatto-Lefever equation for optical frequency combs.[79,118,119]

Regardless of choosing the force density approach or the energy-based (Hamiltonian) one, the derived coupled mode equations and their describing physics should be the same. This will be the case provided that the corresponding forward and backward effects have been properly accounted for in the Hamiltonian. It is fair to say that up to date Brillouin optomechanics experiments are quite accurately described by the electrostrictive and moving boundary effects, and these terms can be derived by exploring only coupled-mode theory and thermodynamics arguments[96]—thus showing that forward and backward effects are directly related to each other in the absence of optical and mechanical dissipation. In other words, photoelasticity is directly related to electrostriction, while moving boundary effect is directly related to radiation pressure. In fact, we discuss later in this tutorial that the overlap integrals describing the forward effects are identical to the those describing the backward effects.[96]

1. Waveguides

Since we aim at a unified discussion of the waveguide and cavity Brillouin optomechanics, we chose to write the coupled mode equations in the form derived in Refs. [90], [113], [114], and [116] for the Stokes wave-interaction. Note that the anti-Stokes also plays an important role in waveguides, especially in the forward intramodal scattering where the almost null wavevectors lead a strong symmetry between the two scattered waves.[114] Nevertheless, considering only the Stokes wave suffices our purpose of discussing the fundamentals of the Brillouin optomechanical coupling. Assuming slowly varying envelopes for the pump ($\tilde{a}_p$), Stokes ($\tilde{a}_s$), and mechanical waves ($\tilde{b}$) (see Appendix A), the following coupled equations are obtained:

$$(v_p\partial_z + \partial_t + v_p\alpha_p/2)\tilde{a}_p = -i\tilde{g}_0\tilde{a}_s\tilde{b}, \tag{7a}$$

$$(\pm v_s\partial_z + \partial_t + v_s\alpha_s/2)\tilde{a}_s = -i\tilde{g}_0^*\tilde{b}^*\tilde{a}_p, \tag{7b}$$

$$[v_m\partial_z + \partial_t + (i\Delta_m + \gamma_m/2)]\tilde{b} = -i\tilde{g}_0^*\tilde{a}_s^*\tilde{a}_p, \tag{7c}$$

where $v_{p,s,m}$ represent the moduli of pump, Stokes, and mechanical group velocities, the upper and lower signs in the ± symbols in Eq. (7b) account explicitly for either copropogating (upper sign) or counterpropagating (lower sign) optical modes,[120] $\alpha_{p,s}$ ([m^{-1}]) are the optical power attenuation coefficient, $\Delta_m = \Omega - \Omega_m$ is the frequency mismatch between the pump-Stokes beating ($\Omega = \omega_p - \omega_s$), $\omega_{p,s}$ represent the pump and Stokes optical frequencies, $\gamma_m = \Omega_m/Q_m$ is the mechanical energy damping rate of a mode with quality factor Q_m, and $\tilde{g}_0$ is the waveguide optomechanical coupling constant. Note that the slowly varying amplitudes in Eq. (7) are normalized such that they represent photons or phonons per unit length of the waveguide[116] [$|a_j|^2$], [$|b|^2$] = m^{-1}, and the coupling constant has SI units of [$\tilde{g}_0$] = (rad/s)$\sqrt{m}$.

The important aspects of the Brillouin interaction follow from Eq. (7).[79,97] The mechanical wave envelope is driven by the beating between the pump and Stokes envelopes, which are slowly varying functions of z under typical values of power and coupling strength.[96,116] In steady-state ($\partial_t \to 0$) and for a small v_m/γ_m ratio (large mechanical damping), a common experimental condition,[71,103] the mechanical wave adiabatically follows the optical drive, $\tilde{b} = -i\tilde{g}_0^*\tilde{a}_s^*\tilde{a}_p/(i\Delta + \gamma_m/2)$. Coupled equations involving only the optical waves can be derived revealing the power-exchange ($P_{p,s} = \hbar\omega_{p,s}v_{p,s}|a_{p,s}|^2$) along the waveguide length,[79,90,96,116,120]

$$\partial_z P_p = -G_B P_p P_s - \alpha_p P_p, \tag{8a}$$

$$\partial_z P_s = \pm G_B P_p P_s \mp \alpha_s P_s, \tag{8b}$$

where we introduced the Brillouin gain coefficient $G_B = 4|\tilde{g}_0|^2\mathscr{L}(\Omega)/(v_s v_p \gamma_m \hbar\omega)$, with $\omega = \omega_p \approx \omega_s$ and $\mathscr{L}(\Omega) = (\gamma_m/2)^2/[(\gamma_m/2)^2 + (\Omega - \Omega_m)^2]$ being the Lorentzian gain profile for a mechanical mode. The gain Lorentzian expresses the role of phase-matching in the Brillouin interaction; if the pump and Stokes frequency are offset from the mechanical mode by more than one mechanical linewidth (γ_m), the Brillouin gain is largely suppressed. In the undepleted pump approximation ($\partial_z P_p \approx 0$), Eq. (8) ensures that the Stokes optical power grows exponentially with a power gain coefficient $G_B P_p$ per unit length, leading to $G_B P_p/\alpha_s > 1$ as the net Brillouin Stokes gain condition. The power exchange interaction described by Eq. (8) is an important property explored in Brillouin amplifiers, filters, and lasers,[121] and other interesting regimes of Brillouin scattering can also be derived from Eq. (7) and have been discussed in detail elsewhere.[84,90,114,116,122–124]

The discussion above shows that within waveguides, the Brillouin gain coefficient G_B is often more relevant than the fundamental optomechanical coupling constant $\tilde{g}_0$. Thus, G_B will be our metric of choice when comparing different waveguides throughout this tutorial. The relation between G_B and the optical and mechanical mode fields can be expressed as[96,125]

$$G_B(\Omega) = Q_m \frac{2\omega_p \mathscr{L}(\Omega)}{\bar{m}_{\text{eff}}\Omega_m^2}\left|\int f_{\text{mb}}^{\text{wg}} dl + \int f_{\text{pe}}^{\text{wg}} dA\right|^2, \tag{9}$$

where Q_m is the mechanical energy quality factor, $\bar{m}_{\text{eff}} = \int\rho|\mathbf{u}_m|^2/\max|\mathbf{u}_m|^2 dA$ is the effective linear mass density of a mechanical mode with displacement profile $\mathbf{u}_m$, ρ is the mass density, and $f_{\text{mb}}^{\text{wg}}$ and $f_{\text{pe}}^{\text{wg}}$ are the line and area overlap integrals representing the MB and PE effects, respectively. We discuss their properties after introducing the optical cavity figure-of-merit expressions. It is important to note that the choice of optical and mechanical mode normalization in the coupled mode-theory affects the expression for the gain, and in Appendix A, we discuss our choices leading to Eq. (9).

2. Cavities

In order to keep the cavity discussion and notation as close as possible to waveguides, we write the cavity coupled mode equations for the slowly varying envelopes for the pump (a_p), Stokes (a_s), and mechanical waves (b) as[79,90]

$$(\partial_t + (i\Delta_p + \kappa_p/2))a_p = -ig_0 a_s b + \sqrt{\kappa_{ep}}s_p, \tag{10a}$$

$$(\partial_t + (i\Delta_s + \kappa_s/2))a_s = -ig_0^* b^* a_p + \sqrt{\kappa_{es}}s_s, \tag{10b}$$

$$[\partial_t + (i\Delta_m + \gamma_m/2)]b = -ig_0^* a_s^* a_p, \tag{10c}$$

where $\kappa_{p,s}$ are the pump and Stokes optical energy damping rates, $\Delta_{p,s} = \omega_{p,s} - \omega_{cp,cs}$ are the frequency detunings between the driving fields ($\omega_{p,s}$) and the cavity modes ($\omega_{cp,cs}$); the optomechanical coupling rate is g_0. The driving field amplitudes are represented by $s_{p,s}$ and coupled to the cavities at a rate $\kappa_{ep,es}$. In writing Eq. (10), we ignored the weak thermal-noise drive for the mechanical modes.[116] The normalization for the optical and mechanical slowly varying amplitudes in Eq. (10) are such that they represent the average number of photons or phonons stored in the cavity,[79] and the coupling constant has SI units of $[g_0] = $ (rad/s).

A plethora of Brillouin optomechanical effects are predicted by Eq. (10),[90] among which lasing is one important example. In this case, it is important to distinguish between optical and mechanical lasing, both of which have been experimentally observed.[33,34,36,72,77,105,126–128] In the mechanical lasing regime,[51,56,127,129] the mechanical mode has a lower dissipation rate ($\Gamma_m \ll \kappa_s$) and experiences the Schawlow-Townes line-narrowing often associated with lasing behavior,[130,131] whereas in the optical lasing regime,[34,36,72,77,105,126] which is often associated with the label *Brillouin laser* due to historical hierarchy, the Stokes mode dissipation is the smallest ($\kappa_s \ll \Gamma_m$) and the linewidth-narrowing is experienced by the Stokes field.[32] One way to see why such dissipation hierarchy defines the lasing field (Stokes or mechanical) is by inspecting Eq. (10) in the undepleted pump approximation: the field experiencing the largest dissipation responds quickly to the interaction terms [proportional to g_0 in right-hand side of Eq. (10)] and can be adiabatically eliminated ($\partial_t \approx 0$). Such adiabatic elimination leaves only one dynamical variable, which is the slowly responding (small dissipation) field, and the lasing threshold occurs when a Hopf bifurcation of the slow field occurs.[132,133] When only a single optical mode is involved, a common situation in many cavity optomechanics experiments,[89] the back-action to the mechanical mode is driven by the sidebands of the pump wave.[89] Two important effects in this single-mode regime are the optical spring,[57,134] amplification[51,135] and cooling[62,136,137] which have been extensively discussed in other reviews.[89,90] A thorough discussion of these effects has been recently published by Safavi-Naeini *et al.*[90] It is also worth mentioning that the pump and Stokes laser frequency detunings in Eqs. (10a) and (10b) impact the cavity dynamics more strongly than those in waveguides (which are nonresonant structures): the steady-state amplitudes for the pump and Stokes fields are attenuated as $|a_{p,s}| \propto |s_{p,s}|^2/\Delta_{p,s}^2$ for large detunings ($\Delta_{p,s} \gg \kappa_{p,s}$), which may cause a substantial increase in the threshold power for Brillouin lasing.[76,138] They also play a very important role in phase-sensitive coherent effects such as electromagnetic induced transparency (EIT), which can be explored to create Brillouin-enabled optomechanical switches[139,140] and nonreciprocal optical devices.[141,142]

Within optical cavities, the most common figure-of-merit is the single-photon optomechanical coupling rate g_0, representing the frequency shift of the optical mode induced by a single quantum of mechanical excitation.[89] Its relation with the optical and mechanical modes can be derived from perturbation theory[100] and is given by

$$g_0 = -\frac{\omega_p x_{zpf}}{2}\left(\int f_{mb}^{cav}\, dA + \int f_{pe}^{cav}\, dV\right),\tag{11}$$

where $x_{zpf} = \sqrt{\hbar/(2m_{eff}\Omega)}$ is the zero-point fluctuation of the mechanical mode with effective mass $m_{eff} = \int\rho|\mathbf{u}_m|^2/\max|\mathbf{u}_m|^2 dV$. f_{mb}^{cav} and f_{pe}^{cav} are the area and volume overlap integrands representing the MB and PE effects, respectively.

3. Cavities vs waveguides

As a final remark on the connection between the distinct figures-of-merit chosen for the cavity and waveguide, it is worth mentioning the so-called optomechanical cooperativity. It is clear that the Brillouin gain G_B depends on mechanical dissipation γ_m, whereas the coupling constants $\tilde{g}_0$ and g_0 do not. For cavities, a condition that is analogous to the net Brillouin gain $G_B P_p > \alpha_s$ is expressed as $C > 1$, where $C = 4g_0^2 n_{cav}/(\gamma_m \kappa_s)$ is the cavity cooperativity, with $n_{cav} = |a_p|^2$ representing the average number of photons stored in the cavity. Although the dissipation hierarchy is distinct for the mechanical or optical lasing discussed above, the condition $C > 1$ represents the lasing threshold condition in both cases.[79] Albeit not so popular, an equivalent waveguide cooperativity ($\tilde{C}$) can also be defined,[79] and similar to cavities, the $\tilde{C} = 1$ condition also represents net waveguide gain $G_B P_p \geq \alpha_s$. Despite the apparent difference between the figures of merit in Eqs. (9) and (11), they can be directly compared to each other if a given waveguide is closed into a path forming an optical cavity —provided that the cavity mode shape resembles the waveguide counterpart as in ring resonators or photonic crystal cavities. For instance, a waveguide with length L_{wg} has an equivalent cavity single-photon coupling rate given by[79,90]

$$|g_0| = |\tilde{g}_0|/\sqrt{L_{wg}} = \left(\frac{v_p v_s \hbar \omega_p \Omega_m}{4L_{wg}Q_m}G_B\right)^{1/2}.\tag{12}$$

In the waveguide examples shown in Fig. 1, we compare the G_B/Q_m calculated from Eq. (9) and the equivalent g_0 from Eq. (12), whereas in the cavity examples, we compare g_0 calculated from Eq. (11) with the equivalent G_B/Q_m obtained from Eq. (12). To avoid specifying the mechanical quality factor for each structure, we quote the Brillouin gain as G_B/Q_m throughout the text examples. To highlight the material dependence of G_B, Appendix B provides a brief discussion on photoelastic Brillouin scaling with material properties.

4. Boundary and volume overlap integrals

The overlap integrals appearing in Eqs. (9) and (11) depend on the spatial behavior of the two integrands arising from the moving boundary and photoelastic perturbations. These are the quantities that we aim to thoroughly discuss in this tutorial. As such, we choose to write the expressions for the Brillouin gain [Eq. (9)] differently from elsewhere[96,125] (see Appendix A for comparison). The moving boundary overlap integrands in Eqs. (9) and (11) are given by[100]

$$f_{mb}^{(cav,\,wg)} = \frac{\mathbf{u}^* \cdot \hat{n}(\delta\varepsilon_{mb}\mathbf{E}_{p,\|}^* \cdot \mathbf{E}_{s,\|} - \delta\varepsilon_{mb}^{-1}\mathbf{D}_{p,\perp}^* \cdot \mathbf{D}_{s,\perp})}{\max(|\mathbf{u}|)N_p^{(cav,\,wg)}N_s^{(cav,\,wg)}},\tag{13}$$

where the permittivity differences are given by $\delta\varepsilon_{mb} = \varepsilon_1 - \varepsilon_2$ and $\delta\varepsilon_{mb}^{-1} = (1/\varepsilon_1 - 1/\varepsilon_2)$ in which $\varepsilon_1 = \varepsilon_0 n_1^2$ and $\varepsilon_2 = \varepsilon_0 n_2^2$ are the permittivities of the guiding material and surroundings, respectively. $\mathbf{u} \cdot \hat{n}$ is the surface-normal component of the displacement vector $\mathbf{u}$; the fields $\mathbf{E}_{j,\|}$ and $\mathbf{D}_{j,\perp}$ are material interface tangential electric and normal displacement fields for the pump ($j = p$) or scattered

(j = s) optical mode. The denominator in Eq. (13) represents the energy or power normalization integrals, $N_i^{cav} = (\varepsilon_0 \int \varepsilon |\mathbf{E}_i|^2 dV)^{1/2}$, $N_i^{wg} = (2\Re(\int \mathbf{E}_i \times \mathbf{H}_i^* \cdot \hat{z} dA))^{1/2}$. It is worth noting that Eq. (13) has dimensions of $[f_{mb}^{wg}]$ = N/W/m² and $[f_{mb}^{cav}]$ = N/J/m², so they represent force surface densities per unit power or energy; therefore, the MB overlap integrals appearing in Eq. (9) for waveguides have dimensions of linear force densities per unit power [N/W/m]; for cavities, the overlap integrals of Eq. (11) have dimensions of force per unit energy [N/J]. This correspondence is expected based on a virtual work principle[69] or following thermodynamic arguments[143] and suggests that understanding the Brillouin optomechanical coupling based on perturbation of the optical fields due to photoelastic and moving boundary effects is equivalent to follow an optical force description when only conservative forces are considered; another way of justifying the appearance of a single coupling coefficient g_0 in Eq. (7) or $\tilde{g}_0$ in Eq. (10) is through the Manley-Rowe relations for the coupled-mode equations,[8,79] which are based on energy conservation among all the waves involved in a lossless nonlinear interaction.[144,145]

The photoelastic overlap integrands in Eqs. (9) and (11) are given by[1]

$$f_{pe}^{(cav, wg)} = \frac{\mathbf{E}_p^* \cdot \delta\varepsilon_{pe}^* \cdot \mathbf{E}_s}{\max(|\mathbf{u}|) N_p^{(cav, wg)} N_s^{(cav, wg)}}, \tag{14}$$

where $\delta\varepsilon_{pe} = -\varepsilon_0 n^4 \mathbf{p}{:}\mathbf{S}$ is the photoelastic tensor perturbation in the permittivity, n is the material refractive index, $\mathbf{p}$ is the photoelastic tensor, and $\mathbf{S} = \nabla_s \mathbf{u}$ is the symmetric strain tensor induced by the mechanical waves, all spatial dependent quantities. Note that by using a symmetric strain tensor, we are assuming a nearly optically isotropic material where the roto-optical effect can be neglected.[146,147] The expression given by Eq. (14) has dimensions of $[f_{pe}^{wg}]$ = N/W/m³ and $[f_{pe}^{cav}]$ = N/J/m³ and represents force volume densities per unit optical power or energy. It worth noting that even though waveguides and cavities are often discussed through distinct figures of merit, they share essentially the same underlying physical mechanisms and therefore share the same coupling expressions of Eqs. (13) and (14), except for the optical mode normalizations. As pointed out by Van Laer et al.,[79] this means that we can anticipate the Brillouin optomechanical coupling in cavities by understanding an equivalent waveguide problem. The material properties used in the simulations discussed here are given in Appendix B.

III. BRILLOUIN COUPLING IN A SILICA GLASS ROD: AN INSIGHTFUL WAVEGUIDE CASE

A silica rod with circular cross section suspended in air represents a simple and instructive platform to understand the fundamentals of Brillouin optomechanical coupling in waveguides. To begin with, analytical solutions are available for both optical[148] and mechanical[149–151] modes, allowing a clear understanding of the modal structure, of its dependence on material properties and waveguide dimensions, and infer symmetry-based selection rules that allow computing coupling coefficients only for relevant modes —more difficult to do in numerical methods. For optical modes, the index contrast between silica and air is high enough to allow strong confinement. Similarly, high-frequency mechanical waves are reflected at the free glass-air interface and form mechanical modes

confined to the glass rod. Experimentally, this structure can be easily fabricated in the form of optical fiber tapers,[152] with diameters ranging from tens of micrometers down to a few hundred nanometers while still exhibiting excellent uniformity along its length;[153] such a platform has been explored recently in a number of Brillouin experiments.[49,74,75,154–156] Intuitively, having both modes confined to the same small region leads to stronger interaction. As we discuss in this section, the physics of Brillouin optomechanical coupling in high-confinement structures is quite more involved and richer,[74,75] to a point that it is even possible to have no interaction whatsoever—an effect we reported recently and referred to as Brillouin self-cancellation.[74]

A. Confined mechanical modes vs plane mechanical waves

We begin discussing the difference in the permittivity perturbation caused by a tightly confined mechanical mode as compared to a simple plane mechanical wave. In bulk, plane longitudinal and transverse (or shear) waves are independent solutions of the mechanical wave equation. A longitudinal mechanical plane wave has only the displacement component $u_z = u_0 e^{-ik_m z}$ along its propagation direction z, where u_0 is a constant amplitude and $k_m = \Omega/V_l$ is the propagation constant at frequency $\Omega/2\pi$; V_l is the longitudinal bulk velocity. This plane wave leads to alternating positive and negative strain layers in the material $S_{zz} = \partial u_z/\partial z = -ik_m u_0 e^{-ik_m z}$, as illustrated in Fig. 4(a). Through the photoelastic effect, these plane strain layers lead to a refractive index grating in the material (homogeneous in the plane transverse to the propagation direction). In waveguides, mechanical modes are generally more complex due to coupling of longitudinal and shear waves at the surface.[149] As a result, the displacement fields in a mode differ significantly from a pure plane longitudinal displacement. In general, a given mode may exhibit all three components u_r, u_ϕ and u_z, and in addition to the dependence on z through the propagating phase $e^{-i\beta_m z}$, each component also varies spatially in the transverse plane (r, ϕ). These mechanical modes exhibit a dispersion relation that detours significantly from the bulk, as shown in Fig. 4(b) for the axial-radial (AR$_{0m}$) and torsional-radial (TR$_{2m}$) mode families; the first subscript indicates the azimuthal number of the mode, while the second one indicates the mode index in order of increasing frequency; Figs. 4(c) and 4(d) illustrate the fundamental modes for these two families. At the cut-off frequency ($\beta_m = 0$), the modes in the axial-radial AR$_{0m}$ family exhibit either radial displacement (u_r) or longitudinal displacement (u_z), and away from the cutoff, they exhibit both displacement components. In addition to the axisymmetric AR$_{0m}$ mode family, we note that for azimuthal index 0 a purely torsional mode family T$_{0m}$ also exists, with only nonzero displacement being u_ϕ[149] (this family is not shown in Fig. 4 for simplicity). The torsional-radial TR$_{2m}$ modes shown in Figs. 4(c) and 4(d) contain all three components u_r, u_ϕ, and u_z. Notice that both of these mode families, T$_{0m}$ and TR$_{2m}$, may induce cross-polarization scattering.[5,10,41,103,154,157–159]

The presence of various displacement components and their complex spatial dependence have two immediate consequences to the Brillouin optomechanical interaction. First, various elements of the strain tensor are generated and their complex spatial profiles cause perturbations in the dielectric permittivity that varies spatially
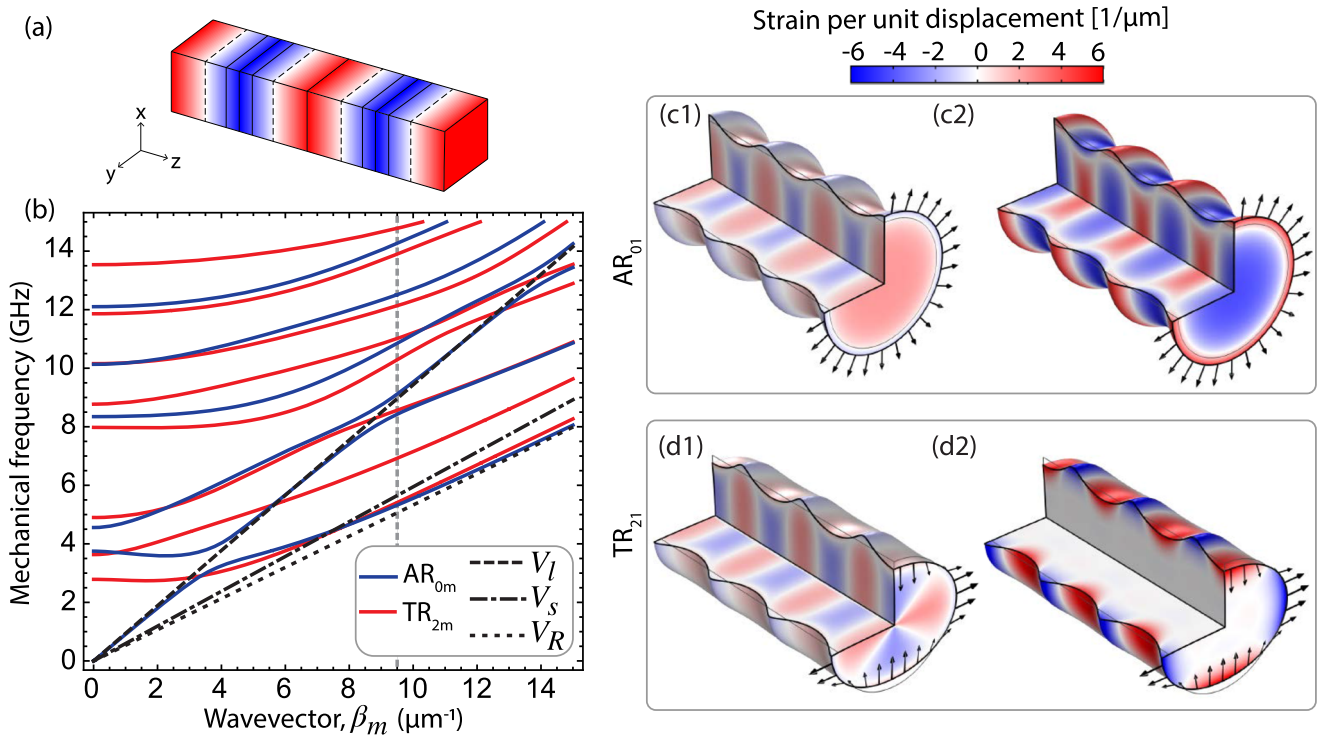
FIG. 4. Strain components of mechanical modes. (a) Schematic of S_{zz} strain of a longitudinal plane wave propagating along the z-direction. (b) Dispersion relation for the AR_{0m} and TR_{2m} modes of a silica rod along with dispersion for a longitudinal (V_l, dashed), shear (V_s, dashed-dotted), and surface-wave Rayleigh wave (V_R, dotted). (c) Calculated S_{rr} strain (c1) and S_{zz} strain (c2) of the fundamental axial-radial mode of a silica rod. (d) Calculated S_{rr} strain (d1) and S_{zz} strain (d2) of the fundamental torsional-radial mode of a silica rod. In (b)–(d), the rod radius was set to $a = 0.5$ μm, and the mechanical wavevector in (c) and (d) was $\beta_m = 9.5$ μm^{-1} [vertical dashed line in (b)], which corresponds to backward intramode scattering phase-matching at $\lambda = 1.55$ μm. A simulation file for parts (c) and (d) is hosted on the data repository.[80]

not only along the propagation direction z but also in the transverse plane (r, ϕ). For example, in the AR_{01} in Fig. 4(c), u_z depends on both (r, z) and thus generates two nonzero strain components: S_{zz}, in analogy to the bulk, as well as S_{zr}. Similarly, u_r depends on both (r, z) and causes S_{rr}, $S_{\phi\phi}$, and S_{rz}. These various strain elements must all be taken into account in the permittivity perturbation tensor, and how well they overlap with the optical modes determines the strength of photoelastic effect. A second consequence of the nature of mechanical modes in waveguides is that in addition to a local perturbation in the dielectric permittivity due to various strain fields, the existence of transverse displacement distorts or shifts the boundary shape of the waveguide. In the example of Figs. 4(c) and 4(d), the AR_{01} mode leads to an increase/decrease in the rod radius while maintaining a circular cross section, while for the TR_{21} modes, the displacement components exhibit a $\cos(2\phi)$ dependence, deforming the cross section from a circular to a somewhat elliptical shape. This shift in the waveguide boundary can also be interpreted as a local and abrupt dielectric permittivity perturbation. For the AR_{01}, a shift outwards of the circular rod boundary is equivalent to an increase in the refractive index from $n_{air} = 1$ (air) to $n_{glass} \approx 1.45$ (glass) in the immediate surrounding region. For the TR_{21}, the index increases in the regions where the core is stretched out and decreases where it contracts. A detailed discussion is provided further in this

section with specific examples illustrating how both manifestations discussed here—presence of spatially varying strain fields and presence of transverse displacement—influence the overall efficiency of the Brillouin optomechanical coupling. One final important comment here is regarding selection rules[160] that determine which families of mechanical modes interact with the optical modes. In a circularly symmetric waveguide, the Brillouin optomechanical coupling coefficients, given by Eqs. (9), (13), and (14), involves azimuthal integrals over $[0, 2\pi]$ of the product of three fields: (i) the pump electric field, (ii) the scattered wave electric field, and (iii) either directly the mechanical displacement field (for the MB effect) or its spatial derivatives (representing strain in the PE effect). In this case, there is a sinusoidal azimuthal dependence for both optical and mechanical modes[148,149] and we can express the azimuthal dependence of the pump, scattered, and mechanical fields as $f(q_p\phi)$, $g(q_s\phi)$, and $h(q_m\phi)$, respectively, where the functions f, g, and h are either cos or sin functions and q_p, q_s, and q_m are integer azimuthal indices. Performing the azimuthal integral results in a necessary condition for nonzero overlap, $q_p - q_s = q_m$ or $q_p + q_s = q_m$. For example, this explains why intramode scattering involving the fundamental optical mode HE_{11}, with azimuthal index $q_p = q_s = 1$, involves only mechanical modes with azimuthal index $q_m = 0$ or $q_m = 2$.

B. Confined optical modes: Boundary field strength and longitudinal component

The moving boundary effect perturbs the dielectric permittivity only near the waveguide glass-air interface. Although the high index difference between glass and air causes large perturbation, its contribution to the Brillouin optomechanical interaction is only relevant if the optical mode extends significantly toward the waveguide boundary. This is the case for a small diameter, as is illustrated in Fig. 5(a) that shows the transverse $|E_t| = \sqrt{|E_r|^2 + |E_\phi|^2}$ and longitudinal $|E_z|$ field profiles (normalized by the maximum of the total field norm), for the y-polarized fundamental mode in a 1 μm diameter rod. In Fig. 5(b), the ratio $|E_t(a)|/|E_t(0)|$ of the electric field strength at the waveguide boundary $r = a$ relative to its value in the center $r = 0$ is plotted as a function of the waveguide diameter. Since the surface discontinuity of the normal electric field E_r leads to an asymmetry in the transverse field profile, to build Fig. 5(b), we chose to evaluate $|E_t(a)|$ along the y-axis *outside* the surface. As the diameter is reduced, the mode expands out toward the surface and eventually its strength at the surface becomes comparable to and even *larger* than its value at the center. This is the regime where the moving boundary is expected to give the most significant contribution to overall Brillouin optomechanical coupling.

Another relevant point in high confinement waveguides is the role of the longitudinal electric field component, E_z, in the Brillouin scattering process. The fundamental optical mode HE_{11} is not purely transverse-electric and always contains the longitudinal components E_z. Figures 5(a) and 5(b) show that for a diameter near the diffraction limit—where mode confinement is maximum—the longitudinal field E_z is comparable to the transverse field E_t. The ratio $\max(|E_z|)/|E_t(0)|$ reaches a maximum of ≈ 0.5 near the diameter of

0.7 μm and decreases too far above or below it as the mode size is significantly increased at these limits. The presence of a strong longitudinal field impacts the optomechanical coupling in waveguides in two ways: first, it is no longer enough to consider the overlap between the permittivity perturbation and the transverse electric field only, but one must also consider the contribution from the longitudinal field in the overlap integrands of Eqs. (13) and (14). Second, and particularly in backward scattering, the longitudinal field changes sign for backward-propagating mode vs forward-propagating mode.[101] This represents a sort of mode mismatch that results in a reduction of the scattering efficiency when compared to the forward case.

C. Brillouin optomechanical coupling

To illustrate how these aspects resulting from the confinement of mechanical and optical modes impact the characteristics of Brillouin optomechanical interaction, we discuss specific examples in detail. We start with the moving boundary effect induced by mechanical modes with different transverse field profiles, covering elements of both forward and backward scattering. We then discuss the more complex photoelastic effect and finally add the contributions from the two effects to obtain the overall Brillouin optomechanical gain. Throughout this discussion, we identify regimes in which one or the other mechanism dominates and regimes in which both contributions are relevant and, combined either constructively or destructively, lead to enhanced or suppressed Brillouin optomechanical interaction, respectively.

1. Moving boundary effect

The optomechanical coupling in a waveguide due to the moving boundary effect, given by Eqs. (9) and (13), involves a line integral along the waveguide boundary. For our case, it is convenient to cast this equation in cylindrical coordinates and directly express the integrand in terms of the electric field components inside the material using $\mathbf{D} = \varepsilon\mathbf{E}$ and in terms of the radial mechanical displacement component u_r (normal to the rod surface). The result is

$$\int f_{mb}^{wg} dl \propto a\varepsilon_0 (n_{glass}^2 - n_{air}^2) \int_0^{2\pi} u_r(a,\phi)$$

$$\times \left[|E_\phi(a,\phi)|^2 + \frac{n_{glass}^2}{n_{air}^2}|E_r(a,\phi)|^2 \pm |E_z(a,\phi)|^2 \right] d\phi, \quad (15)$$

where we have considered both pump and scattered fields propagating in the same transverse optical mode, the $\pm$ sign represents forward and backward scattering, and the proportionality symbol is used to avoid writing the optical and mechanical normalization factors of Eq. (13). The change in sign arises due to the opposite direction of E_z for forward and backward propagating fields. The factor n_{glass}^2/n_{air}^2 multiplying the term containing the normal component of the electric field E_r arises due to the field discontinuity, where we chose to evaluate E_r inside the boundary. For simplicity, we assume that the optical pump and scattered fields propagate in the fundamental HE_{11} mode (y-polarization), for which the azimuthal dependencies are $E_{(r,z)}(a, \phi) = E_{(r,z)} \sin(\phi)$ and $E_\phi(a, \phi) = E_\phi \cos(\phi)$. For the mechanical modes, we consider both families illustrated in Fig. 4, the AR_{0m} and TR_{2m}, the former being circularly symmetric $u_r(a, \phi) = u_r$ and the latter varying as
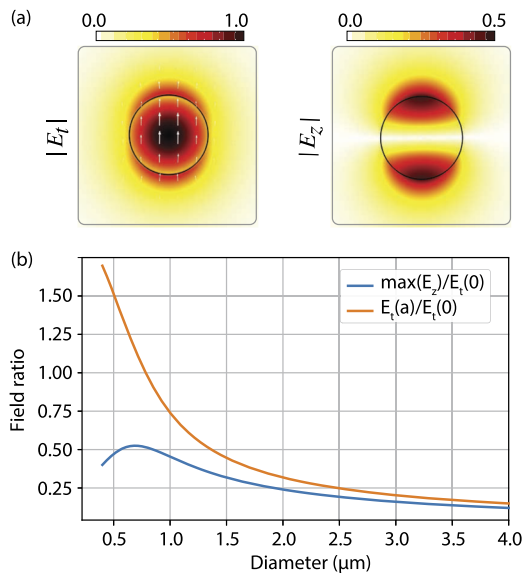

FIG. 5. (a) Optical mode profile (transverse and longitudinal fields, in arbitrary scale) for a 1 μm diameter rod. (b) Ratio of surface-to-center transverse field $|E_t(a)|/|E_t(0)|$ and longitudinal-to-transverse field $\max(|E_z|)/|E_t(0)|$ as a function of diameter. $|E_t(a)|$ is evaluated along the vertical axis in (a) and outside the boundary.

TABLE I. Form of the moving boundary overlap integrals for different modes and scattering directions.

Direction	Mode	$\iint f_{mb}^{wg} dl$
FW	AR_{0m}	$\varepsilon_0(n_{glass}^2 - n_{air}^2)\pi a u_r\left(\frac{n_{glass}^2}{n_{air}^2}|E_r|^2 + |E_\phi|^2 + |E_z|^2\right)$
FW	TR_{2m}	$\varepsilon_0(n_{glass}^2 - n_{air}^2)\frac{\pi}{2} a u_r\left(\frac{n_{glass}^2}{n_{air}^2}|E_r|^2 - |E_\phi|^2 + |E_z|^2\right)$
BW	AR_{0m}	$\varepsilon_0(n_{glass}^2 - n_{air}^2)\pi a u_r\left(\frac{n_{glass}^2}{n_{air}^2}|E_r|^2 + |E_\phi|^2 - |E_z|^2\right)$
BW	TR_{2m}	$\varepsilon_0(n_{glass}^2 - n_{air}^2)\frac{\pi}{2} a u_r\left(\frac{n_{glass}^2}{n_{air}^2}|E_r|^2 - |E_\phi|^2 - |E_z|^2\right)$

$u_r(a, \phi) = -u_r \cos(2\phi)$ (the minus sign is chosen so that the radial displacement is positive along the y-axis for a positive u_r). Here, all fields are evaluated at the waveguide boundary, $u_r = u_r(a)$ and $E_i = E_i(a)$ for $i = r, \phi,$ and z [remembering to evaluate the discontinuous field $E_r(a)$ inside the boundary]. Performing the integral over $[0, 2\pi]$, the result is shown in Table I.

A first observation is that if the longitudinal component E_z is negligible compared to the transverse fields, such as in the bulk or far below and far above the diffraction limit in Fig. 5(b), the results are no different for forward and backward cases. For a 1 μm diameter rod, on the other hand, its impact is significant. The term $|E_z|^2/(n_{glass}^2/n_{air}^2|E_r|^2 + |E_\phi|^2)$ is 0.46, and this factor alone means that the term in parentheses for the AR_{0m} is 2.7 times larger for forward than for backward. For the TR_{2m}, $|E_z|^2/(n_{glass}^2/n_{air}^2|E_r|^2 - |E_\phi|^2) = 2$, and the term in parentheses is 3 times larger in absolute value for forward than for backward.

In Figs. 6(a) and 6(b), we show the results of the moving boundary overlap integral for different mechanical modes for the case of forward scattering. Broadly speaking, we can see that for all modes the overlap integrals increase (in absolute value) as the diameter is

reduced until the diffraction limit is reached, and beyond it, the optical mode expands again, reducing the overall intensity. The overlap integral for the AR_{02} and TR_{21} modes is represented by the blue solid lines (dashed lines for higher order modes) in Fig. 6; note that the AR_{01} mode frequency approaches zero at cutoff (see Fig. 4), and therefore, we chose to plot the AR_{02} in Fig. 6. It is not surprising that the moving boundary contribution is larger for the symmetrical AR_{02} than for the TR_{21}, simply because in the former the entire waveguide boundary shifts outwards (taking positive u_r) causing a positive permittivity perturbation along the complete rod circumference. In the case of TR_{21}, on the other hand, the boundary shifts partially inwards and partially outwards, reducing the net result. It may be surprising that in this case the result is not identically zero, since as the mechanical displacement varies azimuthally with $\cos(2\phi)$ and its integral over $[0, 2\pi]$ is zero. Of course, the integral $\iint f_{mb}^{wg} dl$ involves the overlap of the mechanical displacement with the electric field and not simply the line integral of u_r. The result would be identically zero only if the term $\frac{n_{glass}^2}{n_{air}^2}|E_r|^2 - |E_\phi|^2 + |E_z|^2$ in Table I was zero. The reason this is not the case is a consequence of (i) the field discontinuity at the high-contrast interface, which makes the boundary integral somewhat unbalanced by the term n_{glass}^2/n_{air}^2, and (ii) the presence of a strong longitudinal field. Of course, if we make $n_{glass} \to n_{air}$, all terms in Table I tend to zero as the boundary index difference is reduced. However, the moving boundary contribution tends to zero *faster* for the TR mode relative to AR. This is because moving toward a weakly guidance approximation, the unbalance caused by the field discontinuity tends to disappear as $n_{glass}^2/n_{air}^2 \to 1$ and $|E_\phi|^2 \to |E_r|^2$.

Another instructive example is the moving boundary coupling induced by the fundamental flexural mechanical mode[161] F_{11}, as illustrated in Fig. 7(a). For this mode, $u_r(r = a, \phi) = u_r\cos(\phi)$, and so its perturbation is antisymmetric with respect to the vertical axis in Fig. 7(a). We analyze two cases, intramode scattering $HE_{11} \to HE_{11}$ and intermode scattering $HE_{11} \to HE_{21}$; in all cases, the modes are y-polarized. It is intuitive that an antisymmetric

(a) AR_{02} (solid) and AR_{05} (dashed)   (b) TR_{21} (solid) and TR_{23} (dashed)   (c)

mb — pe — pe+mb

$10^{-2}\ 10^{-3}\ 10^{-4}\ 10^{-5}\ 10^{-6}\ 10^{-7}$ G_B/Q_m (1/W/m)
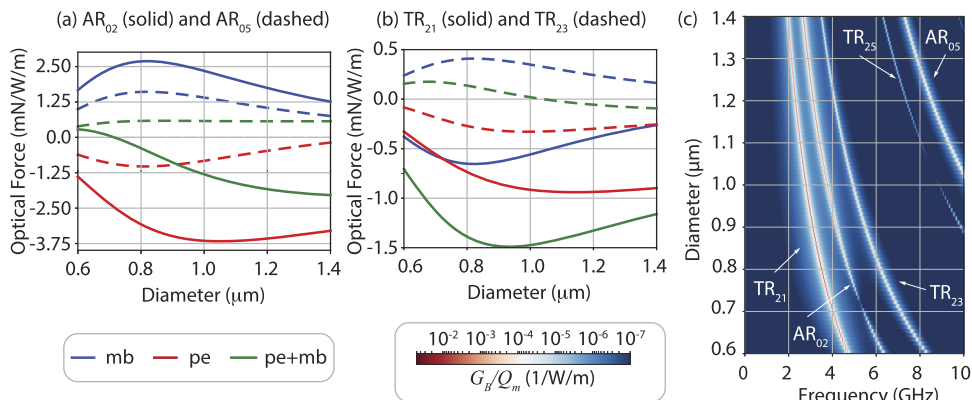
FIG. 6. Overlap integrals for axial-radial modes in (a) and torsional-radial modes in (b), both for forward $HE_{11} \to HE_{11}$ scattering. Contributions from moving boundary (mb, in blue) and photoelastic (pe, in red) effects are shown individually along with their direct sum (green). In (c), the total Brillouin gain $[G_B(\Omega)/Q_m]$ is shown for various mechanical modes as a function of the rod diameter [the linewidth used in the Lorentzian line shape $\mathscr{L}(\Omega)$ was $\gamma_m = \Omega_m/10^3$]. Note that only AR_{02} and AR_{05} appear in (c) since $AR_{0(3,4)}$ are purely longitudinal modes at cutoff. A simulation file for parts (a)–(c) is hosted on the data repository.[80]
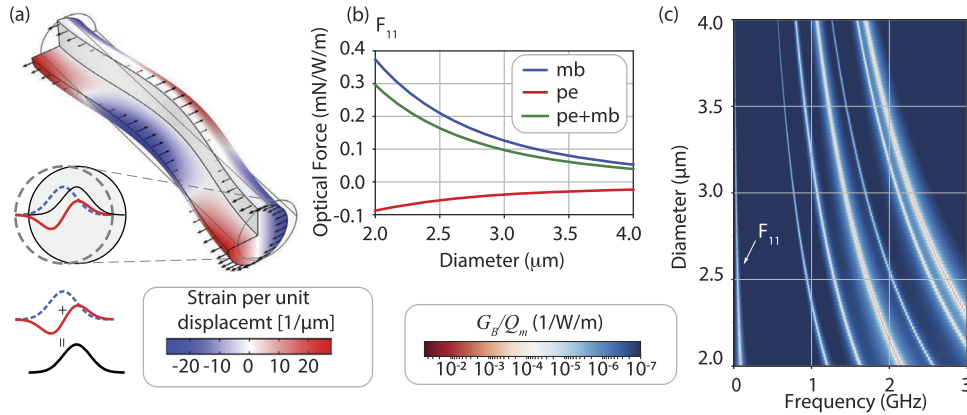
FIG. 7. (a) Fundamental flexural mode in a rod (color represents the S_{zz} strain component). The asymmetric perturbation caused by a lateral shift in the rod cross section induces coupling between the even fundamental HE_{11} mode and the odd HE_{21} mode. (b) Overlap integrals showing contributions from moving boundary (mb, in blue) and photoelastic (pe, in red) effects are shown individually along with their direct sum (green). In (c), the total Brillouin gain $[G_B(\Omega)/Q_m]$ is shown for various high-order flexural modes as a function of the rod diameter [the linewidth used in the Lorentzian line shape $\mathscr{L}(\Omega)$ was $\gamma_m = \Omega_m/10^3$]. A simulation file for parts (a)–(c) is hosted on the data repository.[80]

perturbation should not cause coupling between two symmetric modes, and it is, in fact, the result observed as the line integral $\int\int f_{mb}^{wg} dl$ is zero for both forward and backward cases. As illustrated in Fig. 7(a), a simple lateral shift of the cross section causes an increase in the permittivity on one side and a decrease in the same magnitude on the other side. Since the optical modes involved are symmetric, the overlap integral is zero (note that, differently than the TR_{21} case previously discussed, here the optical field is discontinuous along the vertical axis in Fig. 7, where the perturbation is zero, and therefore has no impact on the result). On the other hand, coupling between the even fundamental HE_{11} mode and the odd high order mode HE_{21} is highly efficient. Mathematically, the azimuthal dependence of the HE_{21} mode is $E_{21,(r,z)}(r = a, \phi) = E_{21,(r,z)} \sin(2\phi)$ and $E_{21,\phi}(r = a, \phi) = E_{21,\phi} \cos(2\phi)$ and so performing the integral over $[0, 2\pi]$ along the rod circumference, the result is

$$\int f_{mb}^{wg} dl \propto \varepsilon_0 (n_{glass}^2 - n_{air}^2) \frac{\pi}{2} a u_r$$

$$\times \left(\frac{n_{glass}^2}{n_{air}^2} E_{21,r}^* E_{11,r} + E_{21,\phi}^* E_{11,\phi} \pm E_{21,z}^* E_{11,z} \right), \quad (16)$$

where again the ± represents the forward and backward scattering, respectively. One way to think about this problem is in terms of local mode expansion as illustrated in Fig. 7(a). The local fundamental mode of the perturbed waveguide (i.e., the shifted rod) is represented by a combination of the HE_{11} and HE_{21} modes in the basis of the unperturbed waveguide. The results of the overlap integral Eq. (16) for F_{11} are shown in Fig. 7(b).

2. Photoelastic effect

The overlap integral we discussed so far for the moving boundary effect is somewhat straightforward in the sense that it involves directly the mechanical displacement. On the other hand, the overlap integral for the photoelastic effect $\int\int f_{pe}^{wg} dA$, where f_{pe}^{wg} is given by Eq. (14), is more complicated because one needs to first understand the strain fields caused by the mechanical displacements and

then combine the different strains to calculate the permittivity perturbation tensor $\delta\varepsilon_{pe}$. This is straightforward for bulk since the longitudinal mechanical plane wave only creates one strain component S_{zz}, and thus, all terms of the permittivity tensor are proportional to S_{zz}. As we mentioned earlier, generally speaking, a mechanical mode may have all displacement components u_r, u_ϕ, and u_z and each one depending not only on z through $e^{-i\beta_m z}$ but also on the transverse components (r, ϕ). Before going to more complex cases, it is instructive to treat intramode forward scattering involving both incident and scattered optical fields in the HE_{11} mode and consider only the azimuthally symmetric mechanical modes AR_{0m}. We can then compare the results of the photoelastic perturbation with the results obtained in Sec. III C 1 for the moving boundary for the same mechanical modes. The phase-matching condition requires the mechanical mode to be at the cut-off point, i.e., $\beta_m = 0$ for the forward scattering. Generally, the azimuthally symmetric mechanical modes exhibit a coupled radial (u_r) and axial (u_z) motion; however, at the cut-off point, one branch becomes purely radial [only $u_r(r)$ is nonzero]. In this case, there are only two nonzero strain components $S_{rr} = \partial u_r/\partial r$ and $S_{\phi\phi} = u_r/r$. Figures 8(a) and 8(b) show the mechanical displacement profiles as well as the strain fields for the fundamental AR_{02} and second order AR_{05}. The fundamental mode exhibits positive displacement in the entire cross section, and the strain fields are almost entirely positive (except for a small radial compression in the outer region). On the other hand, the AR_{02} modes have one node, with positive displacement in the inner core region and negative displacement in the outer region. This leads to positive and negative strain regions.

In the presence of only S_{rr} and S_{zz}, the elements of the permittivity perturbation tensor are

$$\delta\varepsilon_{rr} = -\varepsilon_0 n_{glass}^4 (p_{11} S_{rr} + p_{12} S_{\phi\phi}),$$

$$\delta\varepsilon_{\phi\phi} = -\varepsilon_0 n_{glass}^4 (p_{12} S_{rr} + p_{11} S_{\phi\phi}),$$

$$\delta\varepsilon_{zz} = -\varepsilon_0 n_{glass}^4 (p_{12} S_{rr} + p_{12} S_{\phi\phi}),$$
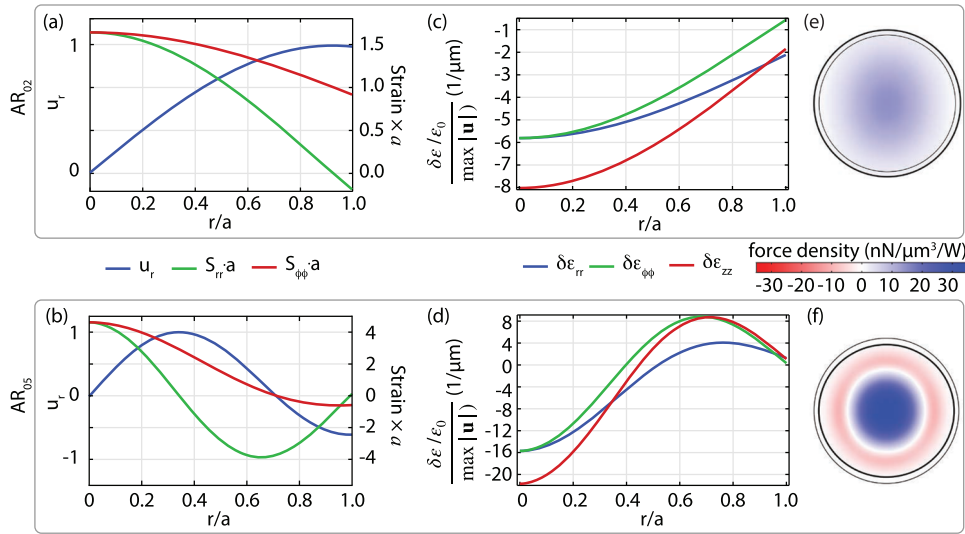
FIG. 8. Radial displacement and strain fields at cutoff ($\beta_m = 0$) for two azimuthally symmetric modes AR_{02} (3.77 GHz) in (a) and for AR_{05} (10.19 GHz) in (b); the blue line represents $u_r/\max(|\mathbf{u}|)$, while the green (red) represents $S_{rr}a/\max(|\mathbf{u}|)$ [$S_{\phi\phi}a/\max(|\mathbf{u}|)$], and $a = 0.5$ μm is the rod radius. The resulting elements of the permittivity perturbation tensor are shown for the same modes in (c) and (d). The integrand in Eq. (17), properly normalized as in Eq. (14), is shown in (e) for AR_{02} with entirely negative perturbation throughout the core and in (f) for AR_{05} with regions of negative and positive perturbation. A simulation file for parts (a)–(f) is hosted on the data repository.[80]

where p_{11} and p_{12} are the photoelastic coefficients for silica (see Table II). Figures 8(c) and 8(d) show all three elements $\delta\varepsilon_{rr}$, $\delta\varepsilon_{\phi\phi}$, and $\delta\varepsilon_{zz}$ for both modes. As the photoelastic coefficients are positive in silica, a region with positive strain (tension) experiences a decrease in the permittivity, while a region with negative strain (compression) experiences an increase. The AR_{02} mode results in negative permittivity perturbation throughout the entire glass cross section; however, the AR_{05} shows regions with positive and negative perturbation. These examples illustrate well that confined mechanical modes exhibit spatial variations in the transverse plane that, in turn, dictates the spatial profile of the permittivity perturbation. One might expect that in the AR_{05} case, these regions of positive and negative perturbation might result in a much lower *average* perturbation for the AR_{02} mode. Although this intuition is correct, the exact result still depends on the spatial overlap between the perturbation profile and the optical mode. This overlap provides a sort of weighting for the positive and negative contributions. In cylindrical coordinates, the PE overlap integral for azimuthal symmetric mechanical modes at the cutoff is

$$\int f_{pe}^{wg}\, da \propto \int \left(\delta\varepsilon_{rr}|E_r|^2 + \delta\varepsilon_{\phi\phi}|E_\phi|^2 + \delta\varepsilon_{zz}|E_z|^2\right) da. \quad (17)$$

All terms in Eq. (17) are dependent on the transverse coordinate, i.e., $E_i = E_i(r, \phi)$ for $i = r, \phi$ and z and $\delta\varepsilon_i = \delta\varepsilon_i(r)$ for $i = rr, \phi\phi$, and zz. Figures 8(e) and 8(f) show the spatial profile of the integrand in Eq. (17) for both modes. As expected, the AR_{02} mode leads to negative permittivity perturbation throughout the entire rod. For the AR_{05} mode, the optical mode being more intense in the center of the rod somewhat favors the negative perturbation region over the positive one, but still a significant positive outer region reduces the net photoelastic effect. The final results of the photoelastic overlap integral for the AR_{02} and AR_{05} modes are shown in Fig. 6(a) (solid and dashed red lines, respectively). For completeness, the results for the TR_{21} and TR_{23} modes are also plotted in Fig. 6(b). Similar to the moving boundary case, the photoelastic overlap integrals increase (in absolute value) as the diameter is reduced until the diffraction

limit and decreases beyond it. As expected, the presence of a node in the AR_{05} mode results in a much weaker photoelastic contribution relative to AR_{02}.

Having discussed individually the contributions from moving boundary and photoelastic effects, we can now compare the results shown in Figs. 6(a) and 6(b) for forward scattering. As mentioned previously, the moving boundary contribution for azimuthal symmetric AR_{0m} modes is always positive. On the other hand, the photoelastic is mostly negative for both modes. The total representing the direct sum of the overlap integrals show that the moving boundary dominates for AR_{05}. For the AR_{02}, the photoelastic dominates for larger diameters while the moving boundary dominates for smaller diameters. Interestingly, one can see that for a diameter of 0.72 μm, the total perturbation is zero as the negative photoelastic contributions exactly cancel out the positive moving boundary contribution. We experimentally demonstrated this Brillouin self-cancellation effect for the case of backward scattering[74] in which the same mechanical wave causes two opposing photoelastic and moving boundary perturbations that cancel out each other. The numerical results show here that this cancellation also occurs for forward scattering. The results for the TR_{21} and TR_{23} modes are shown in Fig. 6(b). For TR_{21}, the two effects add constructively, while for TR_{23}, destructively, including a point of Brillouin self-cancellation around 1 μm. To conclude this discussion on forward scattering, a map of the total intramode $HE_{11} \rightarrow HE_{11}$ forward Brillouin gain spectrum (G_B/Q_m) as a function of the rod diameter is shown in Fig. 6(c). Clearly, only the $AR_{0,m}$ and $TR_{2,m}$ modes appear in the spectrum (only mechanical modes with azimuthal index 0 or 2 contribute to $HE_{11} \rightarrow HE_{11}$). Similarly, a map of the G_B/Q_m for intermode $HE_{11} \rightarrow HE_{21}$ forward Brillouin scattering induced by flexural modes is shown in Fig. 7(c), where only $F_{1,m}$ and $F_{3,m}$ modes appear due to selection rules. In both cases, gains on the order of $G_B/Q_m \approx 10^{-2}$ W^{-1}m^{-1} are observed.

Turning to backward scattering, phase-matching determines that the mechanical propagation constant should be $\beta_m = 2\beta_p$ and thus represents a propagating mechanical mode (i.e., not at the
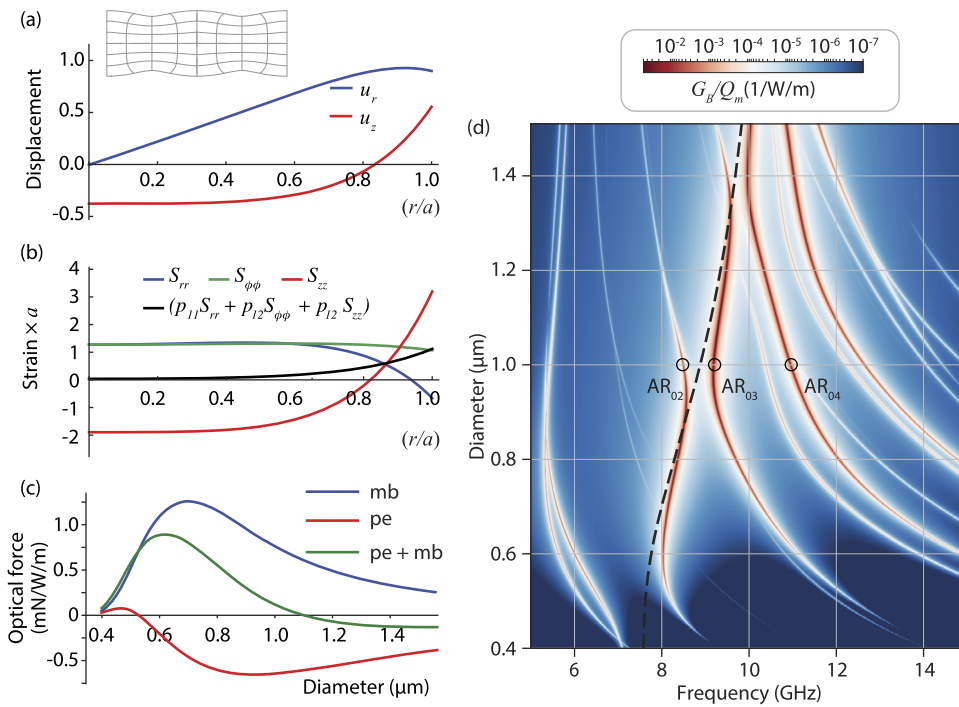
FIG. 9. (a) AR_{01} radial and axial displacement profile for a 1 μm diameter rod (max $|\mathbf{u}|$ normalized) for $\beta_m = 9.5 \ \mu m^{-1}$. The inset shows an illustration of the mechanical deformation. (b) Resulting strain [$S_{ij}a/max(|\mathbf{u}|)$] profiles along with the total strain profile weighted by the photoelastic coefficients. (c) Overlap integral as a function of diameter for $HE_{11} \rightarrow HE_{11}$ backward scattering induced by AR_{01} mode. Blue, red, and green represent moving boundary (mb), photoelastic (pe), and total, respectively. (d) Map of Brillouin gain [$G_B(\Omega)/Q_m$] as a function of diameter for $HE_{11} \rightarrow HE_{11}$ backward scattering, including all mechanical modes in the frequency range shown [the linewidth used in the Lorentzian lineshape $\mathscr{L}(\Omega)$ was $\gamma_m = \Omega_m/10^3$]. Parts (a) and (b) reproduced with permission from Florez *et al.*, Nat. Commun. **7**, 11759 (2016). Copyright 2016 Author(s), licensed under a Creative Commons Attribution 4.0 Unported License. A simulation file for parts (c) and (d) is hosted on the data repository.[80]

cutoff). For $\beta_m \neq 0$, we no longer can decouple u_r and u_z for AR_{0m} modes, as was the case for intramode forward scattering. This is an interesting example because u_r and u_z oscillate out of phase. In other words, an axial compression is usually accompanied by a radial expansion (and vice versa), as shown in Fig. 9(a) for the AR_{01} mode. One can use intuition to expect that these out-of-phase components may lead to opposite photoelastic contributions. The dominant strain fields and their combination to obtain the permittivity perturbation $\delta\varepsilon_{rr}$ are shown in Fig. 9(b). We can observe clearly that the contributions from the transverse strain components S_{rr} and $S_{\phi\phi}$ are mostly opposite to the axial strain S_{zz}. Specifically, note that there is an axial compression (negative strain) in most of the inner core region, but also tension (positive strain) in the outer region. On the other hand, both transverse components are positive (expansion) in the central region, although a bit more complicated at the border. The combination $p_{11}S_{rr} + p_{12}S_{\phi\phi} + p_{12}S_{zz}$ results in an *effective* expansion in the inner core region, leading to negative permittivity perturbation, and an *effective* compression in the outer region, leading to positive perturbation. There are two interesting scenarios to discuss. First, depending on the weighing provided by the overlap with the optical mode, the positive region can indeed exactly cancel out the negative perturbation and the photoelastic contribution becomes zero. For a silica glass rod, this occurs exactly at 0.51 μm diameter as is shown in Fig. 9(c). The second interesting aspect is that the overlap weighting may favor either the positive or negative regions, and the net photoelastic effect can either reinforce the moving boundary effect or oppose it, as shown in Fig. 9(c). In the latter, it is possible that the negative net photoelastic perturbation *exactly* compensates for the positive moving boundary effect, which occurs for the AR_{01} mode at a diameter of 1.1 μm, leading to the Brillouin

self-cancellation effect for backward scattering. A map of the overall backward Brillouin gain spectrum as a function of the rod diameter is shown in Fig. 9(d).

As a final instructive aspect, we discuss how the mechanical mode hybridization, i.e., coupling between purely longitudinal and purely shear waves, impacts the Brillouin optomechanical coupling. The analytical solution for the axial displacement component for azimuthally symmetric modes can be written as the sum of two terms, $u_z = c_1 J_0(k_l r) + c_2 J_0(k_s r)$. The first term represents the contribution from the longitudinal wave to the mode structure and the second from the transverse (shear) wave. Here, c_1 and c_2 are constants, and $k_l = \sqrt{(\Omega/V_l)^2 - \beta_m^2}$ and $k_s = \sqrt{(\Omega/V_t)^2 - \beta_m^2}$ are the transverse wavevectors for the longitudinal and shear components, respectively. Figure 10 shows the plots of u_z for three specific modes indicated as circles in the Brillouin gain map of Fig. 9(d), AR_{02}, AR_{03}, and AR_{04}. These modes have their respective phase-matching frequencies below, almost at, and above the dispersion
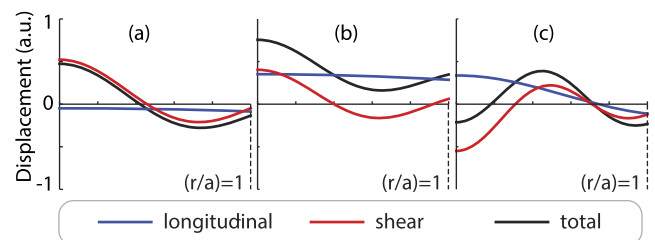
FIG. 10. Longitudinal (blue) and shear (red) components that added together gives the total mechanical displacement u_z (black) for AR_{02} (a), AR_{03} (b), and AR_{04} (c).

curve for a purely longitudinal wave in the bulk [dashed black curve in Fig. 9(d)]. These positions basically determine the *character* of the mode, in other words, the relative contributions of the longitudinal and shear terms to the total displacement field. This can be seen in Fig. 10, where the blue and red curves represent the longitudinal and shear components, respectively, which added together gives u_z (black curve). The AR_{02} sits below the bulk longitudinal dispersion curve, which means its transverse wavevector k_l is imaginary while k_s is real and quite large. As a result, u_z exhibits slow and fast oscillating components in the radial direction. The total mechanical displacement is predominantly given by the shear component and its transverse oscillations reduce the photoelastic effect. On the other hand, the AR_{03} mode sits slightly above the bulk longitudinal dispersion curve, and its transverse longitudinal wavevector k_l is real and very small (its shear component is also real, but quite large). This leads to a mode that, although having both longitudinal and shear components of about the same magnitude, its longitudinal term has practically no transverse oscillation (almost like a plane bulk longitudinal wave!) and therefore exhibits a quite strong photoelastic effect. This is the reason why the mode with a maximum Brillouin gain at a given diameter in the map of Fig. 9(c) is always *following* the longitudinal plane wave dispersion relation. The next AR_{04} mode has large k_l and k_s, and thus, both longitudinal and shear terms oscillate, thus reducing the photoelastic effect.

IV. BRILLOUIN COUPLING IN AXISYMMETRIC MICROCAVITIES

An insight into Brillouin scattering in optical microcavities can be drawn by analyzing the optomechanical interaction in circular symmetric cavities. In this type of cavity, light confinement is well understood using the concept of whispering gallery modes (WGMs).[162] The high orbital angular momentum of the circulating optical field concentrates light at the very edge of the circular symmetric dielectric, where it can propagate with very low radiation losses. In contrast to other light-confinement approaches, such as photonic bandgaps, WGMs can be supported by structures with rather low refractive index contrast—provided the cavity radius is large enough. In microdisk and microring cavities, the association of the whispering gallery effect and the vertical confinement provides the necessary knobs to enhance the strength of the optomechanical interaction. Indeed, this kind of device has not only been the geometry of choice of many cavity nonlinear optics experiments but also the host for landmark experiments in cavity optomechanics and Brillouin scattering.[51,105,126,163]

In the context of the optomechanical interaction, the spatial distribution of optical and mechanical modes is of primary importance.[164,165] As discussed in Sec. II A, the cylindrical symmetry ensures that the optical and mechanical fields will have a propagation phase in the form $\exp(-im\phi + i\omega t)$, where the azimuthal number m is an integer and defines the orbital angular momentum of a given mode and, therefore, its confinement toward the cavity boundary. Important characteristics of optical and mechanical WGMs can be drawn by considering an infinite cylinder cavity.

A. Optical and mechanical radial confinement

The radial confinement of optical WGMs in an infinite dielectric cylinder is a key factor determining the Brillouin

optomechanical coupling and can be easily estimated as follows. The axial optical field (E_z, H_z) radial dependence is given by Bessel functions in the form $J_m(kr)$, where $k = n_{core}k_0$ is the radial wavevector and n_{core} is the cavity dielectric refractive index. If we assume that an optical mode of pth radial order has a node at the cylinder boundary ($r = R$), the resonant wavevectors are given by $k = z_{m,p}/R$ with $z_{m,p}$ being the pth root of $J_m(z)$. Due to their high angular momentum, these modes will penetrate only slightly into the cylinder body. The inner radial position r_i at which the modes begins to fall-off [$J'_m(kr) = 0$] will be given by $r_i = z'_m/k$; z'_m is the first nonzero root of $J'_m(z)$. Under these approximations, we can estimate that the pth radial order optical mode will be confined within the radial region of width $w_r^{opt} = R - r_i = R(1 - z'_m/z_{m,p})$ close to the boundary. Using the approximation $z'_m \approx m$ for large m, we can write

$$w_r^{opt} \approx R(1 - m/z_{m,p}).\tag{18}$$

If we employ the mapping discussed in Sec. II A for the azimuthal numbers ($m \to k_0 n_{eff}R$), Eq. (18) predicts $w_r^{opt} = 700$ nm for fundamental TM-like mode ($n_{eff} \approx 1.8$, $m \approx 35$) of a $R = 5$ μm disk radius silicon microdisk, whereas the TE-like mode ($n_{eff} \approx 2.8$, $m \approx 56$) is predicted to have $w_r^{opt} = 595$ nm. In Fig. 11, we show the full vectorial modes calculated for a silicon microdisk. The simple prediction of Eq. (18) for the modes radial extents are indicated and agrees well with the actual mode profiles. However, the infinite cylinder picture will not capture the full vectorial distribution of the microdisk optical modes highlighted in Figs. 11(b) and 11(c). In analogy to the silica rod, where the out-of-plane z-component of the field is large with respect to the transverse components, the out-of-plane cavity field E_ϕ is also large, relative to the in-plane (E_r, E_z) components,
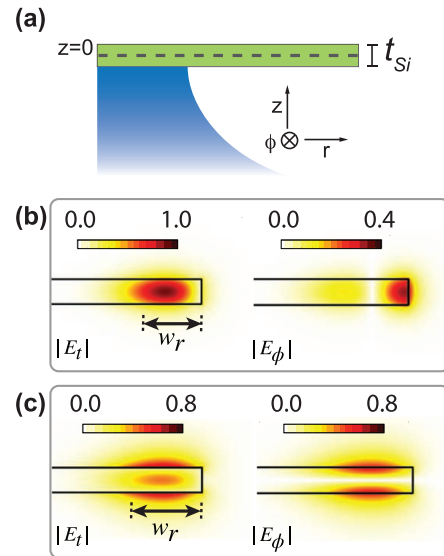
FIG. 11. Optical modes of a silicon microdisk. (a) Schematic of a silicon microdisk cavity with thickness $t = 250$ nm and radius $r = 5$ μm. $(E_r^2 + E_z^2)^{1/2}/\max(|\mathbf{E}|)$ (left) and longitudinal $|E_\phi|/\max(|\mathbf{E}|)$ (right) of (b) TE-like ($m \approx 52$) and (c) TM-like ($m \approx 35$) optical modes calculated at $\lambda = 1.55$ μm. The horizontal double-arrows indicate the radial extent width predicted by Eq. (18), $(w_r^{opt,TE}, w_r^{opt,TM}) \approx (595, 700)$ nm. A simulation file for parts (b) and (c) is hosted on the data repository.[80] Part (a) was adapted from Espinel *et al.*, Sci. Rep. **7**, 43423 (2017). Copyright 2017 AIP Publishing LLC.

in a tightly confining microcavity. This aspect will play a crucial role in the optomechanical coupling integrand as the tangential E_ϕ explicitly appears in the overlap integral of Eqs. (13) and (14).

A similar approach can be evoked to estimate the radial extent of the mechanical WGMs. As in the silica rod waveguide, the coupling of the shear and longitudinal waves at the cylinder's free-surface create hybrid mechanical modes. Each wave component contributes with distinct radial wavevectors $k_{(s,l)} = \Omega/V_{(s,l)}$, and the hybrid mechanical modes will have two characteristic radial extensions,

$$w_r^{(s,l)} \approx R(1 - MV_{(s,l)}/\Omega R), \tag{19}$$

where the subscripts (s, l) indicate transverse (shear) and longitudinal waves. When deriving Eq. (19), we considered that $J_m(k_{(s,l)}R) = 0$ and thus that $k_{(s,l)}R$ is a zero of the Bessel function. Inspecting Eqs. (18) and (19), we notice that optical and mechanical modes may have distinct radial extensions depending on their azimuthal numbers (m, M). Indeed, this simple formula correctly predicts that the phase-matched mechanical modes involved in intramode forward Brillouin scattering [$M = 0$, see Eq. (2)] will be distributed throughout the whole cavity radial extent, i.e., $w_r^{(s,l)} \approx R$; this situation is typical of cavity optomechanics experiments.[51] Such radial spread of the $M = 0$ mechanical modes suggests that they will induce a rather weak radial strain, a simple explanation of why the MB effect is dominant in many WGM cavity optomechanics experiments. This also explains why mechanical radial gratings are needed to confine $M = 0$ mechanical modes toward the edge.[78] Meanwhile, the mechanical modes that are phase-matched for intramodal backward scattering [$M = 2m_p$, see Eq. (2)] will be strongly concentrated at the disk edge. For instance, modes lying very close to the longitudinal or shear bulk velocity lines, $\Omega = MV^{(l,s)}/R$ will be strongly concentrated toward the disk edge ($w_r^{(l,s)} \approx 0$) and should weakly interact with the optical field.

B. Silicon microdisk cavity: An insightful cavity case

Although the rough estimates above help us to understand the role of the whispering gallery effect in the optomechanical overlap, they are only toy-models to the full picture. In order to show interesting properties of more realistic cylindrical symmetry devices, we investigate the Brillouin optomechanical interaction within a single silicon disk. As highlighted in Fig. 11, this device shares many of the whispering gallery characteristics of the infinite cylinder but also the strong vertical confinement typical of high-index contrast integrated photonic devices. We further explore this device as a pedagogical example on how Brillouin optomechanics can be affected in high-index contrast microcavities.

1. Dispersion relation of a silicon microdisk

In order to identify the mechanical modes that can be phase matched with the optical modes in any of the Brillouin configurations described in Sec. II A, we show in Fig. 12(a) the mechanical
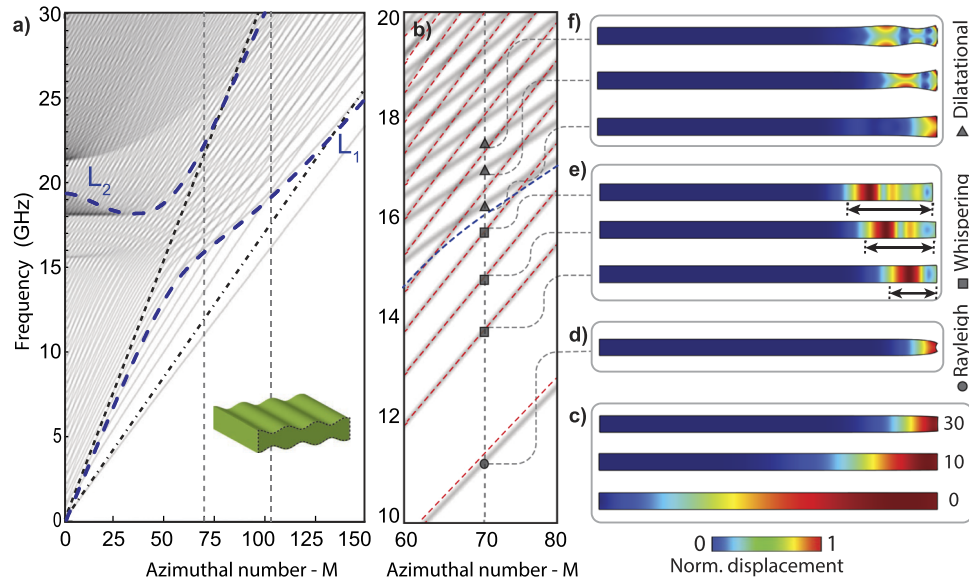
FIG. 12. Mechanical dispersion relation and modes of a silicon disk. (a) Dispersion relation diagram for even mechanical modes (gray curves). The dashed and dashed-dotted black solid lines represent the longitudinal (V_l = 9660 m/s) and transverse (V_t = 5340 m/s) bulk Si mechanical wave velocities. The blue-dashed lines represent the dispersion relation of the first two Lamb modes (L_1 and L_2) of a 250 nm thick silicon slab (inset illustrates d_1 slab mode at $M = 70$). The vertical gray-dashed lines [$M = (70, 104)$] indicate the phase-matching azimuthal number for the (TM, TE) optical modes at 1550 nm, $m_p = M/2 = (35, 52)$. (b) Zoomed-in view the dispersion of the even modes around of $M = 70$. The red dashed lines represent the dispersion of the whispering gallery modes for an infinite cylinder. The blue dashed line is the dispersion of the d_1 slab-mode. The markers along the vertical dashed line refer to representative modes. (c) Radial breathing mode evolving into a surface (Rayleigh) mode as the azimuthal number increases, $M = (0, 10, 30)$. (d) Radial breathing mode in the Rayleigh limit ($M = 70$). (e) First modes of the whispering gallery family; the double-arrows indicate the radial extent predicted for these modes using Eq. (19), $w_r^{(t)} = (650, 955, 1185)$ nm. (f) First modes of the dilatational family. Reproduced with permission from Espinel *et al.*, Sci. Rep. **7**, 43423 (2017). Copyright 2017 Author(s), licensed under a Creative Commons Attribution 4.0 Unported License. A simulation file for part (a) is hosted on the data repository.[80]

dispersion relation of a 250 nm thick silicon-on-air microdisk cavity and some of its representative mechanical modes. Although the dispersion branches in Fig. 12(a) are quite complex, we can understand their behavior by joining the aspects of the mechanical WGMs in an infinite cylinder with the aspects of mechanical Lamb modes in a slab waveguide. There are three mode groups that can be clearly identified; they are the singleton Rayleigh edge (e-mode), dilatational (d-modes), and the whispering gallery (w-modes) and are shown in Figs. 12(d)–12(f). The singleton Rayleigh edge mode originates from the fundamental radial breathing mode (RBM) that concentrates toward the disk edge as the azimuthal number increases; this transition to edge mode is shown in Fig. 12(c). At $M = 0$, Eq. (19) correctly predicts the radial extent of the RBM mode, while it completely fails at large M with negative-valued predictions for the modal radial extent. The physics behind this failure is that the radial breathing mode becomes a surface mode as M increases and shear velocity would need to be replaced by the Rayleigh-wave velocity; this is also clear in Fig. 12(a) where it can be seen to lie below the shear velocity dispersion curve at low azimuthal numbers and move towards the Rayleigh velocity beyond $M \approx 20$. Close to the phase-matching point for the TM-mode ($M = 70$), the RBM is transformed into an edge mode, as shown in Fig. 12(d). Despite the effects of vertical confinement, the e-mode dispersion has a good quantitative agreement with the cylinder surface mode, as highlighted in the zoomed-in view of Fig. 12(b) where the analytical infinite cylinder dispersion relation was overlaid with the disk's. Just above the shear-velocity line, there is also a fantastic agreement with the cylinder dispersion relation, and they are WGM-like (w-modes), shown in Fig. 12(e), with quasi pure radial-azimuthal (u_r, u_ϕ) displacement profiles that are very uniform along the z-direction. The predictions of Eq. (19) for the radial extent of w-modes are very precise, as shown by the double-arrows in Fig. 12(e).

Finally, above the slab Lamb-mode dispersion relation (L_1), dilatational modes with large vertical displacement (u_z) appear. These modes do not exist in an infinite cylinder, but resemble dilatational Lamb modes of a slab. The corresponding slab waveguide used in Figs. 13(a) and 13(b) has the same thickness of the disk and a mapped longitudinal wavevector $\beta_m = M/R$. The first order dilatational mode in Fig. 12(f) is concentrated at the disk edge and move inwards as the frequency increases. The radial extent of these modes can also be predicted by Eq. (19), provided that the mechanical wave velocity is replaced the slab mode velocity—similar to the WGMs modes, dilatational modes lying near the L_1-mode dispersion branch will be closer to the disk edge. This general behavior of modal spatial distribution will be crucial to understand the Brillouin optomechanical coupling which will be discussed next.

2. Brillouin optomechanical coupling in a silicon microdisk

In the intramodal backward scattering, the phase-matching condition requires $M = 2m_p$; therefore, the modes tend to localize toward the edge. In Fig. 13, we show the calculated optomechanical coupling, as given by Eq. (11) for both the TE and TM optical modes shown in Fig. 11. The general behavior of the Brillouin active modes can be better visualized as the cavity thickness is varied, as shown in Figs. 13(a) and 13(b); we highlight the mode groups in Figs. 13(c) and 13(d) following the convention introduced in the previous paragraph (see Fig. 12). Despite the completely distinct geometry, many aspects of these coupling maps still resemble those observed in the silica cylinder waveguide [see Fig. 9(d)]. For instance, we can also roughly predict the position of the shear-like and longitudinal-like modes by overlaying the phase-matching relation $\Omega = 2k_0 n_{\text{eff}} V_{(s,l)}$ to these maps. Around these two curves, represented by white-dashed
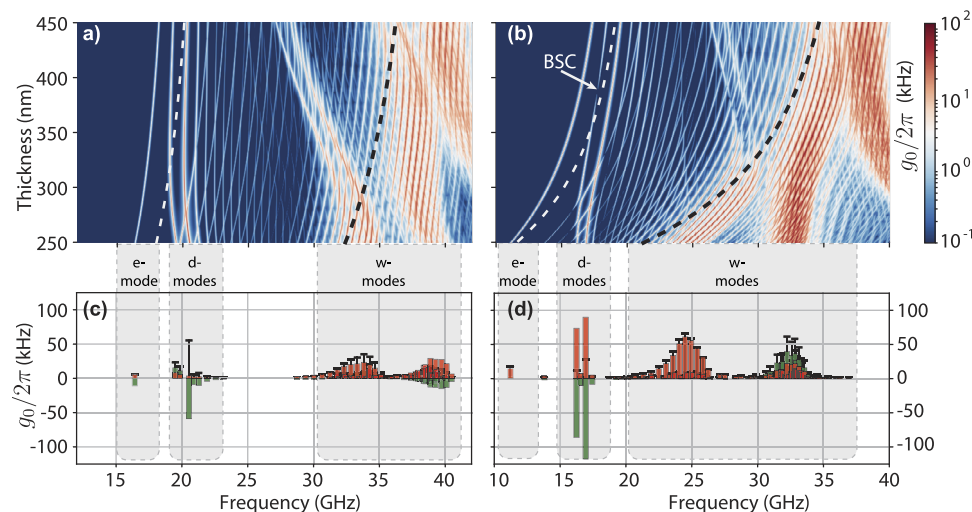
FIG. 13. Optomechanical coupling in a silicon microdisk cavity. Optomechanical coupling rate for (a) TE and (b) TM optical modes as a function of the cavity thickness. In these log-scale maps, each mechanical mode was attributed a Lorentzian profile with a quality factor of 10^3 for aesthetic purposes. The dashed white (black) lines correspond to the expected phase-matching for shear (longitudinal) waves. [(c) and (d)] Optomechanical coupling rate (black bars) between the optical mode and the mechanical even modes [with respect to $z = 0$ plane in Fig. 11(a)] generated by the photoelastic $g_{0,pe}/2\pi$ (red) and moving boundary $g_{0,mb}/2\pi$ (green) contributions; (c) is for TE-mode, while (d) is for TM-mode, both for a 250 nm thick silicon disk; only modes with coupling rates $g_0/2\pi > 1$ kHz are shown. In (c) and (d), the PE contribution is arbitrarily chosen to be positive.

(V_s) and black-dashed (V_l) lines, lie the mode groups with strongest optomechanical coupling.

Below the shear-line dispersion relation, there is the lowest frequency edge mode [Fig. 13(d)], which can be compared to the fundamental axial-radial mode in a cylinder that also becomes a surface mode at large wavenumbers.[75] The dilatational modes [Fig. 12(f)] appear just above the shear-line, which is consistent with their dominantly transverse (shear) ($u_z \gg u_\phi$) components. Toward higher frequencies, the trend observed for the whispering-gallery-like modes [Fig. 12(e)] follows the longitudinal velocity phase-matching curve, showed in dashed-black. A sequence of avoided crossings, similar to the ones observed for the silica rod in Fig. 9(d), is a signature of the scattering being dominated by mechanical modes with strong shear-longitudinal hybridization. This sequence of avoided crossings reflects the mechanical dispersion relation where longitudinal and shear waves couple at free-boundaries of the cavity. The differences between the TE and TM dispersive properties of Figs. 13(a) and 13(b) are mostly due to the distinct optical dispersion relation of these two modes, the TM being steeper at lower thicknesses due its stronger vertical confinement.

In order to get a more quantitative insight on how the two optical modes actually couple to the various families of mechanical modes in a disk cavity, we investigate the components of photoelastic and moving boundary perturbations leading to the results shown in Fig. 13. As expected, due its edge localization, the *e*-mode barely couples to the TE or TM optical mode, despite of being the strongest mode at forward scattering (radial-breathing mode). The first remarkable feature comes with the dilatational (*d*-modes) as we may expect very strong coupling based on their vertical-breathing profile [Fig. 12(f)]. However, when interacting either with TE or TM optical modes, they suffer from the complex interplay between photoelastic and moving boundary effects. In the TE case [Fig. 13(a)], we notice that only the moving boundary effect participates in the overall coupling, whereas in the TM case [Fig. 13(b)], both effects contribute, but with opposite signs. Indeed, at a thickness $t = 360$ nm, the fundamental dilatational mode d_1 suffers from Brillouin self-cancellation (BSC), as indicated in Fig. 13(b).

Since this kind of behavior can completely suppress Brillouin scattering in a given structure, it is instructive to look at all the individual components of the overlap integrals [Eqs. (13) and (14)] contributing to the net optomechanical coupling. We show in Fig. 14(a) the dominant strain components of the d_2-mode (at 16.93 GHz); although this is the phase-matching frequency for the TM-mode, the mode has a similar profile for the TE phase-matching frequency at 20.54 GHz. This mode has not only a large vertical strain S_{zz} but also comparable azimuthal $S_{\phi\phi}$ and shear $S_{r\phi}$ components, as shown in Fig. 14(a). While strain is an important figure, the actual optomechanical coupling still depends on the dielectric permittivity overlap with the optical fields. In order to understand how these components influence the coupling, it is instructive to decompose the PE coupling into components proportional to the tensor elements of the permittivity perturbation $\delta\varepsilon^{ij}$ in Eq. (14), where $ij = (rr, zz, \phi\phi, \phi z, rz, r\phi)$. We show the relative contribution of each photoelastic coupling component, $g_{0,pe}^{ij}/g_0$ of Eq. (14) in Figs. 14(b1) and 14(b2). For the TE mode, the components with significant contribution are $g_{0,pe}^{rr}, g_{0,pe}^{r\phi}$. Using the backward propagating field relation
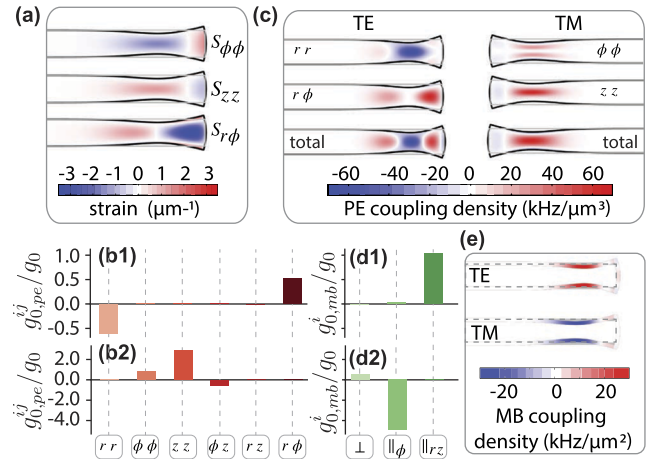
FIG. 14. Dilatational mode (d_2) optomechanical coupling. (a) Dominant normalized strain components for the dilatational mode at 16.94 GHz. (b) Contribution of each coupling term of the PE overlap integral for the TE (b1) and TM (b2) optical modes interacting with the dilatational mode at their respective phase-matching frequencies (16.94 and 20.54 for TM and TE, respectively). (c) Spatial distribution of major PE coupling terms identified in (b1) and (b2) and the total coupling for TE (left) and TM (right). (d) Contribution of each coupling term of the MB overlap integral for the TE (d1) and TM (d2) mode; $\perp$ stands for the boundary normal, $\|_{rz}$ for the in-plane tangential, and $\|_\phi$ for the azimuthal tangential component. (e) Boundary distribution of the total MB coupling. A simulation file for parts (a)–(e) is hosted on the data repository.[80] Parts (a) and (c) were adapted from Espinel *et al.*, Sci. Rep. **7**, 43423 (2017). Copyright 2017 AIP Publishing LLC.

for the backscattered field,[101] $(E_{s,r}, E_{s,\phi}, E_{s,z}) = (E_{p,r}, -E_{p,\phi}, E_{p,z})$, we can write the following expression for the Stokes scattering coupling:

$$g_{0,pe} \approx g_{0,pe}^{rr} + g_{0,pe}^{r\phi} \propto \int |E_{p,r}|^2 \delta\varepsilon_{rr}^* - E_{p,\phi}^* E_{p,\phi} \delta\varepsilon_{r\phi}^* dV,$$

where the minus sign multiplying the azimuthal components is responsible for roughly canceling the photoelastic contribution, as shown in the spatial profile of the total photoelastic contribution in Fig. 14(c). Given this photoelastic effect self-cancellation, the moving boundary term is free to dominate the dilatational mode response, yielding a net coupling of roughly $g_0/2\pi \approx 55$ kHz for the TE mode. The equivalent waveguide gain obtained using Eq. (12) is $G_B/Q_m = 1.5 \times 10^{-1}$ W^{-1}m^{-1}.

It is also instructive to decompose the MB coupling, one in-plane surface-normal contribution $g_{0,mb}^\perp$ and two surface-tangential contributions, one in-plane $g_{0,mb}^{\|_{rz}}$ and one out-of-plane $g_{0,mb}^{\|_\phi}$ involving only the azimuthal optical fields (E_ϕ). The relative moving boundary coupling components are shown in Figs. 14(d1) and 14(d2). As can be noticed in Fig. 14(d1), the moving boundary density contribution for the TE mode is essentially given by the tangential in-plane ($\|_{rz}$) contributions,

$$g_{0,mb} \approx g_{0,mb}^{\|_{rz}} \propto - \int u_z |E_{p,r}|^2 \delta\varepsilon_{mb} r dr,$$

where $\delta\varepsilon_{mb} = \varepsilon_{air} - \varepsilon_{Si}$ is the dielectric permittivity difference between air and silicon, and u_z is the vertical displacement component evaluated the upper or lower disk boundaries. For the mechanical modal phase chosen in Fig. 14, $g_{mb}^{(\|_{rz})}$ is positive because light

perceives a lower effective refractive index as the width shrinks, leading to an increase in the optical frequency. In the TM mode case, the situation is quite different, and the net photoelastic contribution is dominated by two components of the same sign, g_{pe}^{zz} and $g_{pe}^{\phi\phi}$. However, the optical field concentration along the upper and lower boundaries also leads to a very strong negative moving boundary component, which compensates the photoelastic contribution. The physical reason of the negative moving boundary component is the strong azimuthal field along the boundaries, which has a negative sign due to the backscattering configuration,

$$g_{0,mb} \approx g_{0,mb}^{\|_\phi} \propto + \int u_z |E_{p,\phi}|^2 \delta\varepsilon_{mb} r dr.$$

This competition results in rather small coupling of only $g_0/2\pi \approx 27$ kHz ($G_B/Q_m = 8.6 \times 10^{-2}$ W^{-1}m^{-1}). The analysis above further reinforces that the intricate interplay between all the photoelastic components may create unexpected cancellation effects, which could ultimately prevent the optomechanical interaction.

Finally, the mode branches with highest optomechanical coupling are the whispering-gallery modes (w-modes), peaking $g_0/2\pi \approx 66$ kHz at 24.5 GHz ($G_B/Q_m = 3.4 \times 10^{-1}$ W^{-1}m^{-1}) for the TM optical mode. Although the low transverse order w-modes lying close to the shear-velocity curve in Fig. 12(b) have only u_r, u_ϕ displacement components, at higher frequencies—above the slab Lamb mode (L_1) dispersion curve—they exhibit a significant vertical displacement component (u_z). Nevertheless, their u_r, u_ϕ components can still be quantitatively compared to the true whispering gallery modes of an infinite cylinder, as shown in Fig. 15(a). The almost perfect agreement between the $S_{\phi\phi}$ strain in the two geometries allows us to explore the analytical expression for the modal displacement and understand how an oscillatory strain field can lead to such high optomechanical coupling. The azimuthal strain is given by $S_{\phi\phi} = u_r/r - iMu_\phi/r$, by breaking up u_r, u_ϕ into their shear and longitudinal components $u_{(r,\phi)} = u_{(r,\phi)}^{(s)} + u_{(r,\phi)}^{(l)}$, we can also decompose the strain in these components,[76,166,167] $S_{\phi\phi} = S_{\phi\phi}^{(s)} + S_{\phi\phi}^{(l)}$, where $S_{\phi\phi}^{(s)} \propto (J_M(k_s r), J_M'(k_s r))$ and $S_{\phi\phi}^{(l)} \propto (J_M(k_l r), J_M'(k_l r))$. The purely shear component, represented by the blue-dashed line in Fig. 15(b), extends deep into the cylinder, $w_r^s \approx 2750$ nm [as predicted by Eq. (19)], but its fast radial oscillation ($1/k_s \ll w_r^{opt}$) averages out its coupling contribution. The purely longitudinal component, represented by the green-dashed line in Fig. 15(b), does not oscillate significantly and has a shorter penetration $w_r^l \approx 610$ nm predicted by Eq. (19). This is the physical origin of the "bump" seen in the azimuthal strain near the cavity edge, which can also be seen in the strain density maps of Fig. 15(a). This reasoning is confirmed in the relative contribution to the photoelastic optomechanical coupling shown in Fig. 15(c), which confirms that $g_{pe} \approx g_{pe}^{\phi\phi}$ for the w-modes. The role of the u_z displacement component is actually to slightly reduce the photoelastic coupling, through negative $g_{pe}^{\phi z}, g_{pe}^{zz}$, as shown in Fig. 15(c). As for the moving boundary relative contribution, shown in Fig. 15(e), although the longitudinal wave bump contributes to give a tiny tangential in-plane $g_{mb}^{\|_\phi}$ coupling, the small transverse displacement [$u_z \ll (u_r, u_\phi)$] of these modes weakens the MB effect role. A similar discussion applies to the coupling with TE optical modes shown in Figs. 13(a) and 13(c), with the exception of the higher frequencies (around 33.8 GHz) due to phase-matching,
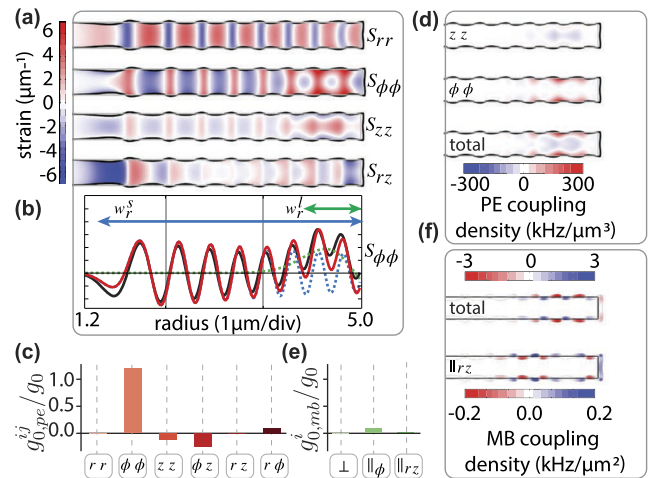
FIG. 15. Whispering gallery mode (w_{16}) optomechanical coupling. (a) Representative normalized strain components for the whispering-gallery mechanical mode at 24.51 GHz. (b) Comparison between microdisk (solid-black) and infinite cylinder (solid-red) azimuthal strain profiles, and the dashed-blue (dashed-green) represents the infinite cylinder shear and longitudinal components; the green and blue arrows are predictions of Eq. (19) for the longitudinal ($w_r^l \approx 610$ nm) and shear components ($w_r^s \approx = 2750$ nm), respectively. (c) Contribution of each coupling term of the PE overlap integral for the TM optical mode. (d) Spatial distribution of major PE coupling terms identified in (b) and the total coupling. (e) Contribution of each coupling term of the MB overlap integral for the TM mode; $\perp$ stands for the boundary normal, $\|_{rz}$ for the in-plane tangential, and $\|_\phi$ for the azimuthal tangential component. (f) Boundary distribution of the total and in-plane tangential $\|_{rz}$ MB coupling. A simulation file for parts (a)–(f) is hosted on the data repository.[80] Part (a) was adapted from Espinel et al., Sci. Rep. 7, 43423 (2017). Copyright 2017 AIP Publishing LLC.

and dominance of the $g_{pe}^{rr}, g_{pe}^{r\phi}$ photoelastic components; in addition, the moving boundary is slightly enhanced by the tangential in-plane $g_{mb}^{\|_{rz}}$ contribution caused by the dominant radial optical field. Overall, the dominance of the azimuthal displacement contribution for the photoelastic effect in cavity w-modes is analogous to what has been discussed in a silica glass waveguide: the photoelastic effect for the mechanical modes lying close the longitudinal wave phase-matching curve ($\Omega = 2k_0 n_{eff} V_l$) is dominated by the out-of-plane displacement component—typical of longitudinal (pressurelike) mechanical modes.

C. Backward Brillouin scattering in other microcavities

Although we focused our microcavity discussion on a silicon microdisk device, we highlighted the structural similarities between the microcavity scattering and the simple silica rod of Sec. III. To further emphasize that the general structure of Brillouin scattering is shared among a variety of structures, we briefly discuss in this section two other popular suspended whispering gallery microcavities, a silica microdisk[168] and a silica microtoroid. The optomechanical coupling evolution, with respect to the disk thickness or toroid minor diameter, is shown in Fig. 16. Both resemble many aspects already discussed in backward scattering within the silica rod waveguide (Sec. III) and the silicon microdisk (Sec. IV). Lower frequency branches appear close to the shear-velocity dispersion
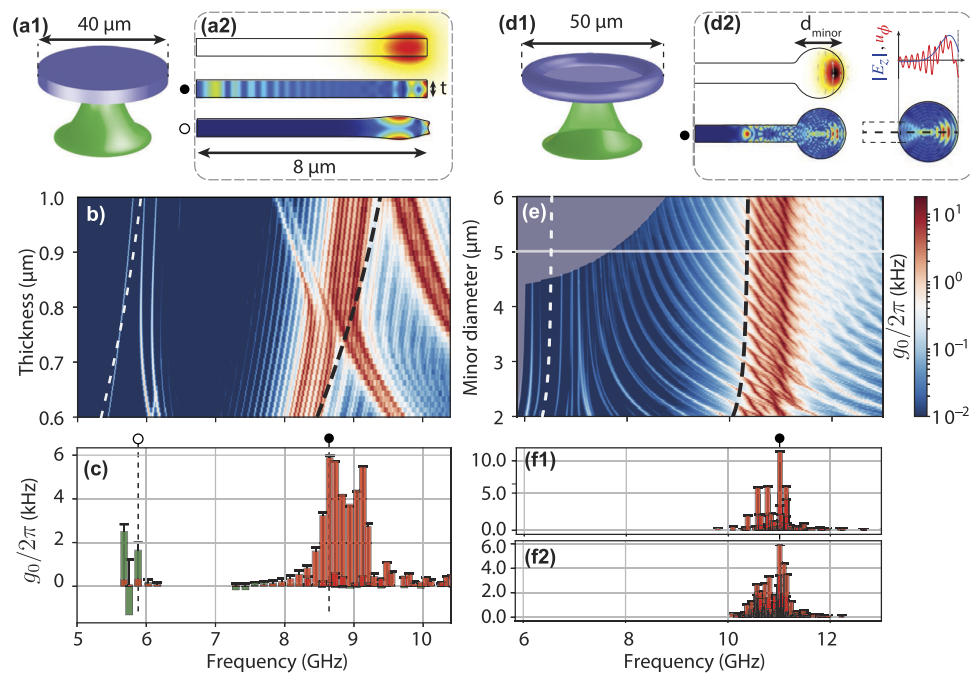
FIG. 16. Optomechanical coupling in a silica microdisk and microtoroid cavities. (a1) Silica microdisk schematics. (a2) (From top to bottom) TM whispering gallery optical mode, whispering gallery mechanical mode, and dilatational mechanical modes that have their optomechanical coupling rate shown in (c). (d1) Silica microtoroid schematics. (d2) (From top to bottom) TM whispering gallery optical mode and higher order axial-radial mechanical modes with the largest optomechanical coupling rate indicated in (f1), the line-cut plots along the toroid equator show the electric-field $|E_z|$ component and u_ϕ displacement. Optomechanical coupling rate for TM mode of (b) a silica microdisk and (e) a microtoroid as a function of the cavity thickness, in these log-scale maps each mechanical mode was attributed a Lorentzian profile with a quality factor of 0.5×10^3; the gray-area in (e) is a spectral region not simulated due to large number of mechanical modes. [(c) and (f)] Optomechanical coupling rate (black bars) between the optical mode and the mechanical even modes [respect to $z = 0$ plane in Fig. 11(a)] generated by the photoelastic $g_{0,pe}/2\pi$ (red) and moving boundary $g_{0,mb}/2\pi$ (green) contributions; (c) is for silica microdisk and (f) for the microtoroid; only modes with coupling rates $g_0/2\pi > 100$ Hz are shown and $g_{0,pe}$ is arbitrarily chosen to be positive. The open and solid circles in parts [(c), (f1), and (f2)] mark the corresponding mode in parts [(a2) and (d2)]. A simulation file for parts [(b)–(e)] is hosted on the data repository.[80]

relation, which tend to concentrate around the dielectric edge, and a higher frequency branch tends to concentrate around the longitudinal velocity dispersion. While the former exhibit a reasonable—or even dominant—contribution from the moving boundary effect, the latter couples essentially due to photoelasticity.

In the silica microdisk, shown in Figs. 16(a1), 16(a2), 16(b), and 16(c), the coupling dependence on the thickness is remarkably similar to the silicon microdisk case of Fig. 13. In the silica microtoroid, shown in Figs. 16(d1), 16(d2), 16(e), 16(f1), and 16(f2), we restricted to analyze minor diameters larger than 2 μm, closer to experimentally demonstrated devices.[77] We verified that the mechanical modes responsible for the scattering peaks around 11 GHz originate from higher order axial-radial modes (similar to those in the silica rod) that were shifted toward the disk edge due their high orbital angular momentum (M). We show in Fig. 16(d2) the mechanical mode profile with largest coupling for a real toroid and an idealized one, where only the circular toroidal region was simulated. Not only there is a remarkable agreement between the two profiles but also the actual coupling spectra, shown in Figs. 16(f1) and 16(f2), are very similar. Yet, the real toroid exhibits a slightly smaller coupling as the mechanical mode hybridizes with displacement along the supporting disk that increases the mode effective mass. As shown in the

line-cut plots of Fig. 16(d2), similar to the silicon disk whispering gallery modes [Fig. 15(a)], on top of the oscillatory azimuthal displacement, the dominant mechanical mode has a slowly varying component due to the longitudinal velocity modal contribution superposed with an oscillatory shear-component. Like in the silicon w-modes of Fig. 15, it is the slowly varying longitudinal component that ensures a net optomechanical coupling. For the sake of shorter computational times, the minor diameter dependence of the optomechanical coupling, shown in Fig. 16(e), was calculated using the idealized toroid. The minor diameter and its range, calculated in Fig. 16(e), are much larger than the microdisk thickness, which is the major reason why it differs from the microdisk coupling map of Fig. 16(b). The larger toroid cross section (shorter frequency interval between mechanical modes) causes the sequence of avoided crossings to appear more frequently in the toroid case. We emphasize that the experimental observation of backward Brillouin scattering within a microtoroid has been recently reported,[77] although the mechanical modes shown here were not identified.

The remarkable similarities of the Brillouin backscattering between the silicon microdisk and microtoroid cavities confirm our initial assertion of the general properties of Brillouin optomechanical coupling in axisymmetric cavities.

D. Bullseye cavity

In forward intramode Brillouin scattering on axisymmetric cavities, the phase match condition is satisfied for $M = 0$ [see Eq. (2)] and leads to a mechanical mode that extends over the entire disk structure, as predicted by Eq. (19). Therefore, initial experiments[163] used the natural confinement of tiny posts on circular and disk-shaped cavities to prevent coupling of the mechanical modes to the necessary bulky and lossy substrates. Nonetheless, optomechanical experiments using many types and shapes of optical and mechanical cavities have been carried out in a large span of applications, from high precision measurements of acceleration[59] and displacement[89] to measurement and generation of nonclassical mechanical states.[62,63,65] Most of these experiments benefit from the simultaneous control of the optical and mechanical fields. In what follows, we will discuss one type of optomechanical cavity, the bullseye optomechanical cavity,[78] which confines optical and mechanical modes through distinct physical mechanisms and allows for independent control of the mechanical and optical properties. As in Sec. IV A, the radial confinement of the optical mode can be understood through WGMs, while the mechanical confinement is achieved by defining an elastic grating along the radial direction in order to create a phononic quasibandgap.

Due to these two edge confinement mechanisms, the bullseye resonator can be understood by analyzing a floating ring structure that is analogous to a bent rectangular waveguide in many aspects. Due to the large refractive index of silicon at 1550 nm, the floating ring structure can have lateral and thickness dimensions of a few hundred nanometers. Like in the silica nanorod, the strong confinement for the optical and elastic waves also increases the photoelastic and moving boundary perturbations. Figure 17(a) shows the dispersion relation for all the mechanical modes that satisfies the intramodal forward scattering ($M = 0$) phase-matching condition of Eq. (2). For each w_{ring}, we calculate all the mechanical modes that couple to the TE optical mode due to the PE and MB perturbations using Eq. (11). The corresponding spectra are normalized such that its peak height is proportional to the total optomechanical coupling rate. Clearly only one mode family, the breathing mode, is dominant in this case. The breathing mode frequency can be estimated assuming that the mechanical wave is confined along the ring width with the velocity of longitudinal waves V_l in bulk silicon. Multiple orders of breathing mode are given by $\Omega_p = p V_l/(2 w_{ring})$, where $V_l = 9660$ m/s and p is an integer representing the mode order. The dashed white lines in Fig. 17(a) represent these estimated mechanical frequency dispersion curves as a function of the ring width for each mode order p. The correct design of the ring and mechanical mode order can be used to either enhance the optomechanical coupling or for self-canceling it. Both situations are analyzed in Figs. 17(b)–17(k). The enhancement of the optomechanical coupling rate between the first order mechanical breathing mode and
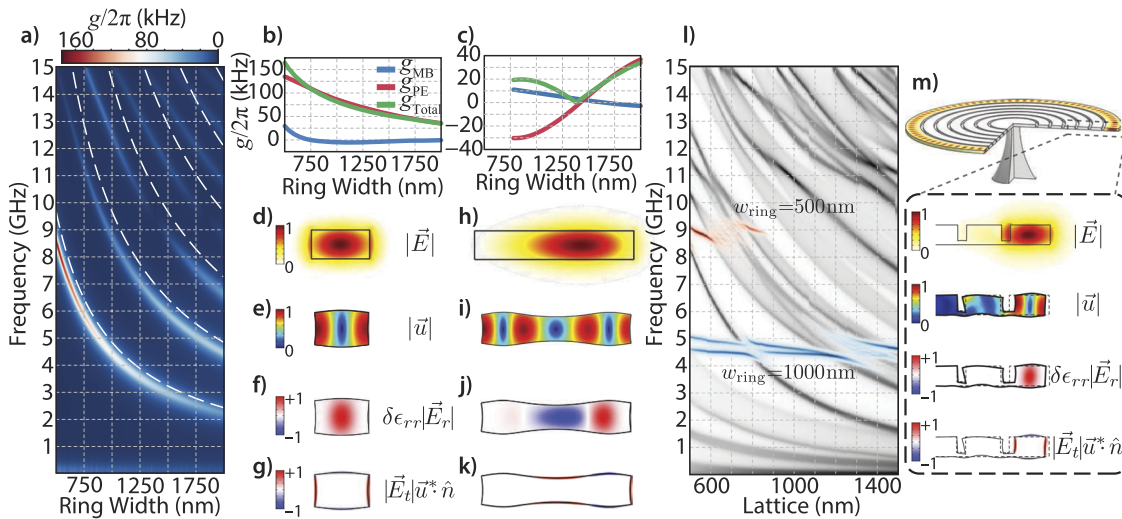
FIG. 17. Optomechanical interaction in a bullseye cavity. In all simulations, the thickness of the silicon layer is 250 nm and the radius of the floating ring or bullseye cavity is 10 μm. (a) FEM simulation of the optomechanical coupling rate for a floating ring structure as a function of its width. The dashed white lines are the calculated frequency for multiple orders of a Fabry-Perot described in the text. [(b) and (c)] Optomechanical coupling rates from the PE (red), MB (blue), and total (green) for the first and third order breathing modes as a function of w_{ring}. (d)–(g): First order breathing mode for w_{ring} = 500 nm. [(h)–(k)] Third order breathing mode for w_{ring} = 1385 nm. [(d) and (h)] The optical mode. [(e) and (i)] Mechanical displacement field for the first and third breathing modes at 8.5 GHz and 9.4 GHz frequencies, respectively. The most relevant contributions for the photoelastic [(f) and (j)] and moving boundary [(g) and (k)] optomechanical coupling contributions are also shown. (l) FEM simulations for the mechanical dispersion relation of a bullseye disk (red and blue shades) as a function of the periodicity for w_{ring} = 500 nm (red shades around 9 GHz) and w_{ring} = 1000 nm (blue shades around 5 GHz). Darker colors refer to larger total optomechanical coupling rates. The gray tone shades are proportional to the mechanical density of states (DOS) of the corresponding linear crystal, where darker regions are related to higher DOS within the mechanical grating. (m) (From top to bottom) Whispering gallery type optical TE mode, closeup of the optical mode, first order breathing mode, and dominant component of the strain (S_{rr}) for the optomechanical coupling rate. All colored FEM simulations are normalized according to the color bars. In the maps of parts (a) and (l), each mechanical mode was attributed a Lorentzian profile with a quality factor of 10^3. A simulation file for part (l) is hosted on the data repository.[80] Part (m) reprinted with permission from Santos et al., Opt. Express 25(2), 508–529 (2017). Copyright 2017 Optical Society of America.

the TE optical mode is due to the fact that both PE and MB contributions have the same sign for w_{ring} smaller than 750 nm. The large optomechanical coupling rate is achieved in this case since the largest strain component (S_{rr}) has almost unit overlap with the optical mode.

On the other hand, self-cancellation is achieved for the coupling between the third order breathing mode and the TE mode around $w_{ring} \approx 1380$ nm, which can be noticed in Fig. 17(a). In this case, like in the silica rod, there is a competition between the photoelastic term (related once again with S_{rr}) and the moving boundary term, as shown in Figs. 17(j) and 17(k). The boundary and volume integrands have exactly opposite phase for this geometry, thus causing the self-cancellation effect. Despite being a very intuitive geometry, the floating ring structure is not feasible. In addition, as we already mentioned, a simple disk is not sufficient to confine the elastic waves towards the disk edge in the intramodal forward scattering regime. Santos et al.[78] discussed in detail a strategy to confine the mechanical waves toward the disk edge using a bullseye type structure. This strategy is very successful and is represented in Fig. 17(l), where both the dispersion relation of the bullseye disk mechanical modes (red and blue shades) and the mechanical density of states (MDOS, gray-shaded) of a 1D-grating are overlaid. Darker gray regions are to be interpreted as higher MDOS within the mechanical grating. The red shaded dispersion relation is for w_{ring} = 500 nm, while the blue shaded dispersion relations are for a w_{ring} = 1000 nm. In both cases, the darker colors represent larger optomechanical coupling (white means zero optomechanical coupling). In both cases, we notice that the existence of the quasi-bandgap (mechanical frequency range with very high reflectivity) not only confines the mechanical modes toward the disk edge but, by doing so, also increases the optomechanical coupling due to the larger overlap between the $\delta\varepsilon_{rr}$ and the optical mode. In Fig. 17(m), we also show the spatial profiles of the major photoelastic and moving boundary components of the radial breathinglike mechanical mode in the full bullseye structure. We notice that despite of the symmetry break in the z-direction (the grating struts are along the bottom part of the disk), which couples the radial u_r and vertical u_z displacement, there is no noticeable difference regarding the origin of the optomechanical coupling between the bullseye disk and the floating ring. These analyses could be easily adapted for other crystalline and compound materials that could be used to form bullseye cavities.

V. PERSPECTIVES AND CONCLUSIONS

Despite remarkable progress in formalizing and unifying the theoretical basis underlying the Brillouin optomechanical interaction in nanophotonics, fundamental and technical aspects are yet to be fully developed, with many opportunities for novel research in this field. In the context of this tutorial, which focused on the two main fundamental interaction mechanisms and the ability to design structures to control both mechanical and optical waves at the nanoscale, there are several new developments still in their early days. In analogy to many unique properties obtained in optical metamaterials, as an example, mechanical metamaterials may offer opportunities to achieve novel properties not available in constituent bulk materials.[169–171] For example, mechanical metamaterials with photoelasticity enhanced beyond that of its constituent materials or metamaterials with complete suppression of photoelasticity. As in optics, mechanical metamaterials may also offer the ability to further design the dispersion relation of mechanical waves.

Anisotropy is also a topic that we barely touched in this tutorial; however, recent progress in using materials such as LiNBO$_3$,[172–175] AlN,[176–178] diamond,[37,179,180] GaAs,[181] and ionic crystals (e.g., CaF$_2$) for optomechanics shows that new design and fundamental challenges are open. Optical anisotropy could significantly modify the photoelastic effect[146] as well as backward effects (forces and torques) accompanying it. Within optical cavities, optical or mechanical anisotropy adds significant constraints in the optomechanical design, for instance, mechanical anisotropy in silicon hazes otherwise simple designs.[78]

As a consequence of a lower crystal symmetry, anisotropy may also be accompanied by other physical effects, such as electro-optic and piezoelectric effects, and enable full electro-optical-mechanical interaction,[90,93,182–184] which shares many of the physical similarities of the discussed devices, displaying both electrostrictive and radiation pressure contributions. Incorporating other nonlinear effects present in semiconductor materials, such as free-carrier absorption, photothermal and photorefractive effects have been pursued theoretically;[185,186] however their possible mitigation or benefit[187,188] for the Brillouin optomechanical interaction is still not fully developed. Despite the large knowledge-base of this field due to technological relevance of electro-optic and acousto-optic modulators, developing effective devices at the subwavelength scale to enable large Brillouin coupling is still underway.

Beyond just the material itself, taking full advantage of periodic structures such as photonic and phononic crystals waveguides and cavities is another area of intense development, both experimentally and theoretically.[45,46,56,57,66,102,103,189] One key aspect of these structures is that they may lead to full confinement of both optical and mechanical defect modes as well as offer mechanisms to mitigate dissipation. In particular, mechanical dissipation[190] is still hindered by the large number of mechanical modes and their inherent coupling caused by geometrical imperfections or residual stress in fabricated structures. Along the same lines, opportunities for designing defect-robust structures—such as by exploring mechanical topological insulators—is an exciting new area.[191–193]

A whole new quantum horizon for Brillouin optomechanics may arise when feasible device designs and improvement on microfabrication processes enable experimental demonstrations within the strong couple interaction limit, at which light and sound hybridize to form a coupled entity,[90] with initial works focusing on reducing optical[194] and mechanical dissipation[183,195–197] or enhancement of the effective coupling strength.[87,194,198] Finally, multimode Brillouin optomechanical interaction[64,199] can lead to exquisite results where interference between multiple mechanical modes coupled to an optical mode can mitigate extrinsic loss mechanisms,[200] extending optical delay through electromagnetically induced transparency[201] and creating highly coherent mechanical modes.[202] In its simpler form, where distinct optical modes couples a single mechanical mode,[203] cooling and amplification in continuous media[204] can be explored and mediate coupling between distinct optical and mechanical modes.[205]

Although we described the Brillouin interaction using energy arguments—instead of force densities—it is worth emphasizing how such force densities depend on the electromagnetic stress-tensor and momentum density, and their impact in the Brillouin optomechanical coupling described in this tutorial. These choices have been at the core of the century-old Abraham-Minkowski controversy,[206–208] and while major progress has been made on this controversy,[209–211] some aspects of the debate are still alive[212–214] and it was not the goal of this tutorial to resolve them. In the context of cavity optomechanics, for example, there are several articles that derive the optical force, which acts upon the cavity mechanical degree of freedom, following the convention[51,215,216] of photon momentum given by $\hbar k$ (k being the wavevector *within* the dielectric defining the optical cavity). Although not explicitly mentioned in most articles, this convention is consistent with the Minkowski approach[217] and ensures a match between the force calculated using a momentum picture[217] and the more widespread energy picture, which uses a virtual-work argument to derive the optical force for an adiabatic (slowly varying) mechanical degree of freedom.[217–221] Those descriptions and their success in predicting experimental results (such as optical spring effect and cooling[89]) may suggest that the optomechanics community has taken the Minkowski side. However, it is worth mentioning Nelson's perspective[222] where he argues that although the light momentum is partially carried by the vacuum and material response fields, it is the sum of both—coined by him as *wave momentum*—that is given by $\hbar k$ per photon in the quantum regime. It is also mentioned that apart from material dispersion, the *wave momentum* represents the Minkowski one, a perspective that has been previously pointed out by Van Laer.[223] Finally, from a macroscopic electrodynamics perspective, the difference between the force densities calculated using either Abraham or Minkowski formalisms should differ by a time-oscillatory term[208,224,225] (known as the Abraham force) that averages out with optical monochromatic fields. It is precisely this term that explicitly appears in Wolff's coupled-mode theory derivation[96] as the "moving polarization" effect. Similar to the history of the moving boundary perturbation, first proposed by Johnson,[100] and its connection to radiation pressure boundary forces, the discovery of the "moving polarization" term as an additional force strengthens the idea that approaching the problem from different perspectives may grasp us into new physics; however, due to its scaling as the ratio of mechanical to optical frequencies,[96] it has yet to find an experiment that could probe it.

In summary, we discussed in detail how the photoelastic and moving boundary effects interplay to enhance or suppress the Brillouin optomechanical interaction in nanophotonic structures. Its general structure in both forward and backward scattering configurations was discussed based on pedagogical case studies. Albeit emphasis was given to specific examples, we highlighted the underlying general structure of the Brillouin coupling. This investigation also revealed that the Brillouin self-cancellation effect is present in many structures in both forward and backward interaction and should be carefully considered in nanophotonic device design. Also our numerical simulations identified the mechanical modes responsible for backward scattering in a silica microtoroid. By providing the simulation files used in preparing this tutorial[80]—developed in a widely used commercial solver—we hope to encourage and shorten the path for students and researchers initiating their investigation in this exciting field.

APPENDIX A: COUPLED MODE EQUATIONS ANSATZ AND RELATION BETWEEN GAIN EXPRESSIONS

The expression for the waveguide Brillouin gain in Eq. (9) was derived by Wolff *et al.* in Ref. 96 using the coupled-wave theory formalism. Their ansatz for the waveguide slowly varying fields is such that the slowly varying envelopes are dimensionless and the optical and mechanical modal fields carry on their respective SI units. In contrast to Ref. 96, we choose to write the waveguide coupled-wave equations in Eq. (7) following the normalization adopted in Refs. 69 and 90 and the cavity equations in Eq. (10) following their usual normalization;[79,89,90] these choices not only keep the optical and mechanical equations symmetric but they also provide a connection between the waveguide and cavity couplings. However, if one wants to keep the actual physical dimensions of the optical and mechanical fields, which is the case when using a commercial mode solver such as COMSOL Multiphysics, the choice in Ref. 96 is very convenient. In Refs. 96 and 115, the Brillouin gain [$W^{-1}m^{-1}$] is written as

$$G_B^{\text{Wolff}} = \frac{2\omega_p \Omega_m |Q_{\text{SBS}}|^2}{P_s P_p P_m \alpha_m} \frac{\alpha_m^2}{\alpha_m^2 + \delta\beta^2}, \tag{A1}$$

where Q_{SBS} is the total SBS coupling coefficient ($[Q_{\text{SBS}}] = $ J m^{-1}) and can be interpreted as work per unit length;[96] $\alpha_m = \gamma_m/(2v_m)$ is the mechanical displacement attenuation ($[\alpha_m] = $ m^{-1}) (the factor 2 is due to the connection between displacement and energy dissipation); $\delta\beta = \beta_m - (\beta_s - \beta_p)$ is the wavevector mismatch; $P_{p,s,m}$ represents the power carried in the pump, Stokes, or mechanical modes. Q_{SBS} in Eq. (A1) is calculated from the field profiles [see Eqs. (33) and (41) in Ref. 96] and is subject to whatever normalizations are carried out in the mode solver of choice; for instance, in COMSOL, the fields are normalized either through the finite-element mass matrix or by their norm maximum. Since we wanted to compare the coupling integrals among different geometries in this tutorial, we found instructive to incorporate the normalizing powers appearing in the denominator of Eq. (A1) into the coupling expression. Furthermore, since the mechanical Poynting theorem[149] ensures the relation $P_m = \mathcal{E}_m v_m$ between the power, the linear energy density ($\mathcal{E}_m$), and the group velocity (v_m) of the mechanical wave,

$$G_B^{\text{Wolff}} = 4\omega_p Q_m \frac{(\gamma_m/2)^2}{(\gamma_m/2)^2 + (\Delta_m)^2}\left(\frac{|Q_{\text{SBS}}|^2}{P_s P_p \mathcal{E}_m}\right), \tag{A2}$$

where we converted the spatial attenuation and wavevector mismatch to the dissipation rate and frequency detuning by employing $\alpha_m = \gamma_m/(2v_m)$ and $\Delta_m = \Omega - \Omega_m = v_m \delta\beta$, together with $\gamma_m = \Omega_m/Q_m$. The rightmost quantity in parentheses in Eq. (A2) is independent of normalization and could be directly used to compare different structures. However, because the mechanical energy scales as the frequency squared ($\mathcal{E}_m = 2\Omega_m^2 \int \rho |\mathbf{u}_m|^2 dA$), such a quantity would favor modes with low-frequency and hinder the actual spatial optomechanical overlap that is solely dependent on the mode field profiles. To remove this frequency dependence, we introduce the effective mass linear density $\bar{m}_{\text{eff}} = \int \rho |\mathbf{u}_m|^2 / \max(|\mathbf{u}_m|^2) dA$ so that

$$G_B^{\text{Wolff}} = Q_m \frac{2\omega_p \mathcal{L}(\Omega)}{\bar{m}_{\text{eff}}\Omega_m^2} \left(\frac{|Q_{\text{SBS}}|^2}{P_s P_p \max(|\mathbf{u}_m|^2)} \right), \quad \text{(A3)}$$

where the Lorentzian lineshape defined in Eq. (8) was introduced. Given that the optical power is calculated from the modal fields as $P_i = 2\Re(\int \mathbf{E}_i \times \mathbf{H}_i^* \cdot \mathbf{z} dA) = (N_i^{\text{wg}})^2$, where N_i^{wg} is defined in Eq. (13), it shows the equivalence between Eq. (9) and the expressions employed in Refs. 96, 115, 125, and 226. Therefore, the surface force densities in Eq. (13) and volume force densities in Eq. (14) are related to integrands in $Q_{\text{SBS}} = \int q_{\text{SBS}}^{\text{mb}} dl + \int q_{\text{SBS}}^{\text{pe}} dA$ as

$$f_{(\text{mb, pe})}^{(\text{wg})} = \frac{q_{\text{SBS}}^{(\text{mb, pe})}}{\max(|\mathbf{u}_m|)N_p^{\text{wg}}N_s^{\text{wg}}}. \quad \text{(A4)}$$

Finally, it important to mention that the finite-element solver employed throughout this tutorial adopts the $\exp(-i\beta z + i\omega t)$ ansatz in the *RF Electromagnetic Waves* and *Structural Mechanics* modules. This is very important as the sign of all the expressions involving the z-derivative of mechanical fields, e.g., strain tensor, depend on this convention. Therefore, the modal expansion leading to Eq. (A1) and consistent with COMSOL's ansatz is given by

$$\mathscr{F}_{\text{wg}}(\mathbf{r}, t) = \tilde{a}(z)\mathbf{F}(\mathbf{r}_t)\exp(-i\beta z + i\omega t) + c.c., \quad \text{(A5a)}$$

$$\mathscr{F}_{\text{cav}}(\mathbf{r}, t) = a(t)\mathbf{F}(\mathbf{r}_t)\exp(-im\phi + i\omega t) + c.c., \quad \text{(A5b)}$$

$$\mathscr{U}_{\text{wg}}(\mathbf{r}, t) = \tilde{b}(z)\mathbf{u}(\mathbf{r}_t)\exp(-i\beta_m z + \Omega t) + c.c., \quad \text{(A5c)}$$

$$\mathscr{U}_{\text{cav}}(\mathbf{r}, t) = b(t)\mathbf{u}(\mathbf{r}_t)\exp(-iM\phi + \Omega t) + c.c., \quad \text{(A5d)}$$

where $\mathscr{F}$ denotes either an electric or magnetic field and $\mathbf{F}(\mathbf{r}_t)$ denotes their modal vector fields depending only on the transverse coordinates; $\mathscr{U}$ denotes the mechanical displacement field, while $\mathbf{u}(\mathbf{r}_t)$ is the modal vector field; $a(z)$ and $a(t)$ [$b(z)$ and $b(t)$] are the dimensionless slowly varying optical (mechanical) field amplitudes. Since COMSOL preserves the SI units of the modal fields, the normalization employed in the discussion of the coupled-mode equations [Eq. (7)] is distinct from Eq. (A5). The advantage of COMSOL normalization is that one can keep track of the dimensions of each quantity in the gain expressions [Eqs. (9), (11), (13), and (14)].

APPENDIX B: MATERIAL PROPERTIES

In our calculations, the material properties shown in Table II were used.[227,228] Despite silicon being anisotropic and there are different directions, the purpose of this tutorial was worth considering an isotropic approximation. This particular choice of parameters does not affect the general behavior of the Brillouin optomechanical interaction discussed here. One may expect, however, that genuine

TABLE II. Material properties used in the simulations.

Physical property	Si	SiO$_2$	As$_2$S$_3$
Refractive index n	3.5	1.45	2.37
Density ρ (kg/m^3)	2329	2203	3210
Young modulus Y (GPa)	170	73.1	16.2
Poisson ratio ν_P	0.28	0.17	0.285
Photoelastic tensor p_{11}	−0.09	0.121	0.25
Photoelastic tensor p_{12}	0.017	0.27	0.24
Photoelastic tensor p_{44}	−0.0535	−0.0745	0.005

cylindrical symmetry breaks down in this material and modal patterns should be affected, which does not prevent the observation of Brillouin optomechanical coupling in such structures.[78] Nonetheless, in order to provide the reader with an example of the use of anisotropic material and to better compare our simulations with Refs. 71 and 125, we simulate the under-etched waveguide shown in Fig. 1(e) aligned along a $\langle 110 \rangle$ axis. In this case, the elasticity (c_{11}, c_{12}, c_{44}) = (166, 64, 79) GPa and photoelasticity (p_{11}, p_{12}, p_{44}) = (−0.09, 0.017, −0.051) matrices were rotated by $\pi/4$ around the crystal z-axis (100 direction).[149]

The photoelastic contribution to the Brillouin gain has a strong dependence on the properties of several materials. In order to compare the Brillouin gain performance of different materials using Eq. (9), it is worth making a few approximations. We assume (i) intramodal scattering so $N_p^{\text{wg}} = N_s^{\text{wg}}$, (ii) the mechanical mode is uniform and perfectly confined to a spatial region of area A_m such that

$$\bar{m}_{\text{eff}} = \int \rho |\mathbf{u}_m|^2 / \max |\mathbf{u}_m|^2 dA \approx \rho A_m. \quad \text{(B1)}$$

Within these approximations, the overlap integrands in Eq. (14) can also be simplified and written as

$$\int f_{\text{pe}}^{\text{wg}} dA \approx -\frac{n^4 \bar{p} \tilde{S}}{c} \frac{\int_n |\mathbf{E}_p|^2 dA}{2 \int_\infty n|\mathbf{E}_p|^2 dA}, \quad \text{(B2)}$$

where $\bar{p}$ is an effective photoelastic constant associated with the average normalized strain field $\tilde{S} = S/\max(|u_m|)$, and the relation $(N_p^{\text{wg}})^2 = 2\Re(\int \mathbf{E}_p \times \mathbf{H}_p^* \cdot \mathbf{z} dA) \approx 2cn\varepsilon_0|\mathbf{E}_p|^2$ was used, implicitly assuming a plane-wave-like optical mode. The numerator integral in Eq. (B2) is carried out only in the "guiding" region where the optical mode is confined. Further assuming that the optical field is uniform and distributed in the guiding region of refractive index n, Eq. (B2) simplifies to $\int f_{\text{pe}}^{\text{wg}} dA \approx -n^3 \bar{p} \tilde{S}/(2c)$. Using these approximations, Eq. (9) can be written as

$$G_B(\Omega) \approx Q_m \frac{\omega_p n^6 \bar{p}^2 \tilde{S}^2}{2c^2 \rho A_m \Omega_m^2} \mathcal{L}(\Omega). \quad \text{(B3)}$$

From Eq. (B3), one may derive the usual bulk backward Brillouin gain expression[120] by assuming a purely longitudinal normalized mechanical strain, $\tilde{S}^2 = \beta_m^2$, $\bar{p} = p_{12}$ $\Omega_m = \beta_m V_l$ (V_l is longitudinal velocity), and $Q_m = \beta_m V_l/\gamma_m$. With the backward phase-matching condition $\beta_m = 2\omega_p n/c$,

$$G_B(\Omega) \approx \frac{1}{A_m} \left(\frac{\omega_p^2 n^7 p_{12}^2}{c^3 V_l \rho \Gamma_m} \right) \mathcal{L}(\Omega). \quad \text{(B4)}$$

The quantity in parentheses is often referred to as peak Brillouin gain g_B [m/W].[120] Note that some authors prefer to eliminate the longitudinal velocity [$V_l = \Omega_m c/(2\omega_p n)$], which results in a n^8 dependence of the peak Brillouin gain. By isolating the material properties in g_B, we find that it scales as

$$(c^3/\omega_p^2)g_B = \left(\frac{n^7 p_{12}^2}{V_l \rho \Gamma_m} \right),$$

demonstrating that materials with large refractive indices and photoelastic constants, and low mechanical velocity and dissipation are desirable in determining the strength of the Brillouin interaction. Given such scaling, it is not surprising that in the examples of Fig. 1, silicon and As_2S_3 display the largest gains. Silicon, despite the small photoelastic constants, has the largest refractive index, while As_2S_3 has a reasonable refractive index and a large photoelastic constant and low mechanical velocities. Mechanical dissipation is another important aspect revealed by g_B; this is an advantage of crystalline materials, such as silicon, which may have very low mechanical dissipation at low temperatures.[195,229]

REFERENCES

[1] A. Yariv and P. Yeh, *Optical Waves in Crystals: Propagation and Control of Laser Radiation* (John Wiley and Sons, New York, NY, 1983).

[2] L. Brillouin, *La Diffraction de la Lumière par des Ultra-Sons, Actualités Scientifiques et Industrielles* (Hermann et Cie, 1933).

[3] E. P. Ippen and R. H. Stolen, Appl. Phys. Lett. **21**, 539 (1972).

[4] K. O. Hill, B. S. Kawasaki, and D. C. Johnson, Appl. Phys. Lett. **28**, 608 (1976).

[5] N. L. Rowell, P. J. Thomas, H. M. van Driel, and G. I. Stegeman, Appl. Phys. Lett. **34**, 139 (1979).

[6] N. Rowell, V. C. Y. So, and G. I. Stegeman, Appl. Phys. Lett. **32**, 154 (1978).

[7] A. Gaeta and R. Boyd, Phys. Rev. A **44**, 3205 (1991).

[8] R. W. Boyd, *Nonlinear Optics*, 3rd ed. (Academic Press, 2008).

[9] A. B. Ruffin, in *Technical Digest: Symposium on Optical Fiber Measurements, 2004* (IEEE, 2004), pp. 23–28.

[10] R. M. Shelby, M. D. Levenson, and P. W. Bayer, Phys. Rev. B **31**, 5244 (1985).

[11] E. M. Dianov, A. V. Luchnikov, A. N. Pilipetskii, and A. N. Starodumov, Opt. Lett. **15**, 314 (1990).

[12] J. K. Jang, M. Erkintalo, S. G. Murdoch, and S. Coen, Nat. Photonics **7**, 657 (2013).

[13] K. Y. Song, M. G. Herráez, and L. Thévenaz, Opt. Express **13**, 9758 (2005).

[14] Y. Okawachi, M. S. Bigelow, J. E. Sharping, Z. Zhu, A. Schweinsberg, D. J. Gauthier, R. W. Boyd, and A. L. Gaeta, Phys. Rev. Lett. **94**, 153902 (2005).

[15] Z. M. Zhu, D. J. Gauthier, and R. W. Boyd, Science **318**, 1748 (2007).

[16] D. Marpaung, C. Roeloffzen, R. Heideman, A. Leinse, S. Sales, and J. Capmany, Laser Photonics Rev. **7**, 506 (2013).

[17] D. Marpaung, B. Morrison, R. Pant, and B. J. Eggleton, Opt. Lett. **38**, 4300 (2013).

[18] D. Marpaung, B. Morrison, M. Pagani, R. Pant, D.-Y. Choi, B. Luther-Davies, S. J. Madden, and B. J. Eggleton, Optica **2**, 76 (2015).

[19] R. Pant, D. Marpaung, I. V. Kabakova, B. Morrison, C. G. Poulton, and B. J. Eggleton, Laser Photonics Rev. **8**, 653 (2014).

[20] J. Li, H. Lee, and K. J. Vahala, Nat. Commun. **4**, 2097 (2013).

[21] D. M. Nguyen, B. Stiller, M. W. Lee, J. C. Beugnot, H. Maillotte, A. Mottet, J. Hauden, and T. Sylvestre, IEEE Photonics Technol. Lett. **25**, 94 (2013).

[22] O. Shlomi, E. Preter, D. Ba, Y. London, Y. Antman, and A. Zadok, Opt. Express **24**, 26867 (2016).

[23] E. Preter, D. Ba, Y. London, O. Shlomi, Y. Antman, and A. Zadok, Opt. Express **24**, 27253 (2016).

[24] D. M. Chow, Z. Yang, M. A. Soto, and L. Thévenaz, Nat. Commun. **9**, 2990 (2018).

[25] A. Zarifi, B. Stiller, M. Merklein, Y. Liu, B. Morrison, A. Casas-Bedoya, G. Ren, T. G. Nguyen, K. Vu, D.-Y. Choi, A. Mitchell, S. J. Madden, and B. J. Eggleton, J. Opt. Soc. Am. B **36**, 146 (2019).

[26] J. M. S. Domingo, J. Pelayo, F. Villuendas, C. D. Heras, and E. Pellejer, IEEE Photonics Technol. Lett. **17**, 855 (2005).

[27] S. Preussler, A. Wiatrek, K. Jamshidi, and T. Schneider, IEEE Photonics Technol. Lett. **23**, 1118 (2011).

[28] G. Bahl, K. H. Kim, W. Lee, J. Liu, X. Fan, and T. Carmon, Nat. Commun. **4**, 1994 (2013).

[29] Y. Antman, A. Clain, Y. London, and A. Zadok, Optica **3**, 510 (2016).

[30] J. Li, M.-G. Suh, and K. J. Vahala, Optica **4**, 346 (2017).

[31] L. F. Stokes, M. Chodorow, and H. J. Shaw, Opt. Lett. **7**, 509 (1982).

[32] A. Debut, S. Randoux, and J. Zemmouri, Phys. Rev. A **62**, 023803 (2000).

[33] J. Li, H. Lee, and K. J. Vahala, Opt. Lett. **39**, 287 (2014).

[34] W. Loh, S. Yegnanarayanan, F. O'Donnell, and P. W. Juodawlkis, Optica **6**, 152 (2019).

[35] N. T. Otterstrom, R. O. Behunin, E. A. Kittlaus, Z. Wang, and P. T. Rakich, Science **360**, 1113 (2018).

[36] S. Gundavarapu, G. M. Brodnik, M. Puckett, T. Huffman, D. Bose, R. Behunin, J. Wu, T. Qiu, C. Pinho, N. Chauhan, J. Nohava, P. T. Rakich, K. D. Nelson, M. Salit, and D. J. Blumenthal, Nat. Photonics **13**, 60 (2018).

[37] R. J. Williams, Z. Bai, S. Sarang, O. Kitzler, D. J. Spence, and R. P. Mildren, e-print arXiv:1807.00240v1 (2018).

[38] R. G. Smith, Appl. Opt. **11**, 2489 (1972).

[39] P. Dainese, P. S. J. Russell, N. Joly, J. C. Knight, G. S. Wiederhecker, H. L. Fragnito, V. Laude, and A. Khelif, Nat. Phys. **2**, 388 (2006).

[40] A. Kobyakov, S. Kumar, D. Q. Chowdhury, and A. B. Ruffin, Opt. Express **13**, 5338 (2005).

[41] P. Dainese, P. S. J. Russell, G. S. Wiederhecker, N. Joly, H. L. Fragnito, V. Laude, and A. Khelif, Opt. Express **14**, 4141 (2006).

[42] J. C. Beugnot, T. Sylvestre, H. Maillotte, G. Melin, and V. Laude, Opt. Lett. **32**, 17 (2007).

[43] J. C. Beugnot, T. Sylvestre, E. Carry, H. Maillotte, G. Melin, S. Lempereur, A. Fleureau, and V. Laude, Proc. SPIE **7357**, 73570S (2009).

[44] D. Elser, U. L. Andersen, A. Korn, O. Glöckl, S. Lorenz, C. Marquardt, and G. Leuchs, Phys. Rev. Lett. **97**, 133901 (2006).

[45] M. S. Kang, A. Butsch, and P. S. J. Russell, Nat. Photonics **5**, 549 (2011).

[46] M. S. Kang, A. Nazarkin, A. Brenn, and P. S. J. Russell, Nat. Phys. **5**, 276 (2009).

[47] A. Butsch, J. R. Koehler, R. E. Noskov, and P. S. J. Russell, Optica **1**, 158 (2014).

[48] G. Bashan, H. H. Diamandi, Y. London, E. Preter, and A. Zadok, Nat. Commun. **9**, 2991 (2018).

[49] D. M. Chow, J.-C. Beugnot, A. Godet, K. P. Huy, M. A. Soto, and L. Thevenaz, Opt. Lett. **43**, 1487 (2018).

[50] M. L. Povinelli, M. Lončar, M. Ibanescu, E. J. Smythe, S. G. Johnson, F. Capasso, and J. D. Joannopoulos, Opt. Lett. **30**, 3042 (2005).

[51] T. Carmon, H. Rokhsari, L. Yang, T. J. Kippenberg, and K. J. Vahala, Phys. Rev. Lett. **94**, 223902 (2005).

[52] M. Li, W. H. P. Pernice, C. Xiong, T. Baehr-Jones, M. Hochberg, and H. X. Tang, Nature **456**, 480 (2008).

[53] G. Anetsberger, R. Rivière, A. Schliesser, O. Arcizet, and T. J. Kippenberg, Nat. Photonics **2**, 627 (2008).

[54] G. Anetsberger, O. Arcizet, Q. P. Unterreithmeier, R. Rivière, A. Schliesser, E. M. Weig, J. P. Kotthaus, and T. J. Kippenberg, Nat. Phys. **5**, 909 (2009).

[55] M. Li, W. H. P. Pernice, and H. X. Tang, Nat. Photonics **3**, 464 (2009).

[56] Q. Lin, J. Rosenberg, X. Jiang, K. J. Vahala, and O. J. Painter, Phys. Rev. Lett. **103**, 103601 (2009).

[57] M. Eichenfield, R. Camacho, J. Chan, K. J. Vahala, and O. J. Painter, Nature **459**, 550 (2009).

[58] G. S. Wiederhecker, L. Chen, A. Gondarenko, and M. Lipson, Nature **462**, 633 (2009).

[59] A. G. Krause, M. Winger, T. D. Blasius, Q. Lin, and O. J. Painter, Nat. Photonics **6**, 768 (2012).

[60]M. Zhang, G. S. Wiederhecker, S. Manipatruni, A. Barnard, P. McEuen, and M. Lipson, Phys. Rev. Lett. **109**, 233906 (2012).

[61]M. Bagheri, M. Poot, L. Fan, F. Marquardt, and H. X. Tang, Phys. Rev. Lett. **111**, 213902 (2013).

[62]J. Chan, T. P. M. Alegre, A. H. Safavi-Naeini, J. T. Hill, A. Krause, S. Gröblacher, M. Aspelmeyer, and O. J. Painter, Nature **478**, 89 (2011).

[63]A. H. Safavi-Naeini, J. Chan, J. T. Hill, T. P. M. Alegre, A. Krause, and O. J. Painter, Phys. Rev. Lett. **108**, 033602 (2012).

[64]G. S. Agarwal and S. S. Jha, Phys. Rev. A **88**, 013815 (2013).

[65]R. Riedinger, S. Hong, R. A. Norte, J. A. Slater, J. Shang, A. G. Krause, V. Anant, M. Aspelmeyer, and S. Gröblacher, Nature **530**, 313 (2016).

[66]A. H. Safavi-Naeini, S. Gröblacher, J. T. Hill, J. Chan, M. Aspelmeyer, and O. J. Painter, Nature **500**, 185 (2013).

[67]S. Hong, R. Riedinger, I. Marinković, A. Wallucks, S. G. Hofer, R. A. Norte, M. Aspelmeyer, and S. Gröblacher, Science **358**, 203 (2017).

[68]R. Pant, E. Li, D. Y. Choi, C. G. Poulton, S. J. Madden, B. Luther-Davies, and B. J. Eggleton, Opt. Lett. **36**, 3687 (2011).

[69]P. T. Rakich, C. Reinke, R. Camacho, P. Davids, and Z. Wang, Phys. Rev. X **2**, 011008 (2012).

[70]H. Shin, W. Qiu, R. Jarecki, J. A. Cox, R. H. Olsson III, A. Starbuck, Z. Wang, and P. T. Rakich, Nat. Commun. **4**, 1944 (2013).

[71]R. Van Laer, B. Kuyken, D. Van Thourhout, and R. Baets, Nat. Photonics **9**, 199 (2015).

[72]B. Morrison, A. Casas-Bedoya, G. Ren, K. Vu, Y. Liu, A. Zarifi, T. G. Nguyen, D.-Y. Choi, D. Marpaung, S. J. Madden, A. Mitchell, and B. J. Eggleton, Optica **4**, 847 (2017).

[73]E. Giacoumidis, A. Choudhary, E. Magi, D. Marpaung, K. Vu, P. Ma, D.-Y. Choi, S. Madden, B. Corcoran, M. Pelusi, and B. J. Eggleton, Optica **5**, 1191 (2018).

[74]O. Florez, P. F. Jarschel, Y. A. V. Espinel, C. M. B. Cordeiro, T. P. Mayer Alegre, G. S. Wiederhecker, and P. Dainese, Nat. Commun. **7**, 11759 (2016).

[75]J. C. Beugnot, S. Lebrun, G. Pauliat, H. Maillotte, V. Laude, and T. Sylvestre, Nat. Commun. **5**, 5242 (2014).

[76]Y. A. V. Espinel, F. G. S. Santos, G. O. Luiz, T. P. M. Alegre, and G. S. Wiederhecker, Sci. Rep. **7**, 43423 (2017).

[77]Y. Honda, W. Yoshiki, T. Tetsumoto, S. Fujii, K. Furusawa, N. Sekine, and T. Tanabe, Appl. Phys. Lett. **112**, 201105 (2018).

[78]F. G. S. Santos, Y. A. V. Espinel, G. O. Luiz, R. S. Benevides, G. S. Wiederhecker, and T. P. Mayer Alegre, Opt. Express **25**, 508 (2017).

[79]R. Van Laer, R. Baets, and D. Van Thourhout, Phys. Rev. A **93**, 053828 (2016).

[80]G. Wiederhecker, P. Dainese, and T. P. Mayer Alegre (2019). "Data repository for the tutorial paper 'Brillouin optomechanics in nanophotonic structures,'" data repository, Zenodo. https://doi.org/10.5281/zenodo.1971811

[81]A. Kobyakov, M. Sauer, and D. Chowdhury, Adv. Opt. Photonics **2**, 1 (2010).

[82]Z. Bai, H. Yuan, Z. Liu, P. Xu, Q. Gao, R. J. Williams, O. Kitzler, R. P. Mildren, Y. Wang, and Z. Lu, Opt. Mater. **75**, 626 (2018).

[83]B. J. Eggleton, C. G. Poulton, and R. Pant, Adv. Opt. Photonics **5**, 536 (2013).

[84]M. Merklein, A. Casas-Bedoya, D. Marpaung, T. F. S. Büttner, M. Pagani, B. Morrison, I. V. Kabakova, and B. J. Eggleton, IEEE J. Sel. Top. Quantum Electron. **22**, 336 (2016).

[85]M. Maldovan, Nature **503**, 209 (2013).

[86]E. Garmire, New J. Phys. **19**, 011003 (2017).

[87]N. Dostart, S. Kim, and G. Bahl, Laser Photonics Rev. **9**, 689 (2015).

[88]V. Laude and J.-C. Beugnot, AIP Adv. **3**, 042109 (2013).

[89]M. Aspelmeyer, T. J. Kippenberg, and F. Marquardt, Rev. Mod. Phys. **86**, 1391 (2014).

[90]A. H. Safavi-Naeini, D. Van Thourhout, R. Baets, and R. Van Laer, Optica **6**, 213 (2019).

[91]M. Winger, T. D. Blasius, T. P. M. Alegre, A. H. Safavi-Naeini, S. Meenehan, J. Cohen, S. Stobbe, and O. J. Painter, Opt. Express **19**, 24905 (2011).

[92]K. Van Acoleyen, J. Roels, P. Mechet, T. Claes, D. Van Thourhout, and R. Baets, IEEE Photonics J. **4**, 779 (2012).

[93]A. Pitanti, J. M. Fink, A. H. Safavi-Naeini, J. T. Hill, C. U. Lei, A. Tredicucci, and O. J. Painter, Opt. Express **23**, 3196 (2015).

[94]R. Van Laer, R. N. Patel, T. P. McKenna, J. D. Witmer, and A. H. Safavi-Naeini, APL Photonics **3**, 086102 (2018).

[95]Q. Liu, H. Li, and M. Li, Optica **6**, 778 (2019).

[96]C. Wolff, M. J. Steel, B. J. Eggleton, and C. G. Poulton, Phys. Rev. A **92**, 013836 (2015).

[97]C. Wolff, B. Stiller, B. J. Eggleton, M. J. Steel, and C. G. Poulton, New J. Phys. **19**, 023021 (2017).

[98]C. Wolff, P. Gutsche, M. J. Steel, B. J. Eggleton, and C. G. Poulton, J. Opt. Soc. Am. B **32**, 1968 (2015).

[99]D. F. Nelson and M. Lax, Phys. Rev. B **3**, 2778 (1971).

[100]S. G. Johnson, M. Ibanescu, M. A. Skorobogatiy, O. Weisberg, J. D. Joannopoulos, and Y. Fink, Phys. Rev. E **65**, 066611 (2002).

[101]M. Mrozowski, *Guided Electromagnetic Waves: Properties and Analysis*, Computer Methods in Electromagnetics Series (Research Studies Press, 1997).

[102]A. Brenn, G. S. Wiederhecker, M. S. Kang, H. Hundertmark, N. Joly, and P. S. Russell, J. Opt. Soc. Am. B **26**, 1641 (2009).

[103]M. S. Kang, A. Brenn, and P. S. J. Russell, Phys. Rev. Lett. **105**, 269908 (2010).

[104]V. Laude, A. Khelif, S. Benchabane, M. Wilm, T. Sylvestre, B. Kibler, A. Mussot, J. M. Dudley, and H. Maillotte, Phys. Rev. B **71**, 045107 (2005).

[105]M. Tomes and T. Carmon, Phys. Rev. Lett. **102**, 113601 (2009).

[106]H. E. Engan, B. Y. Kim, J. N. Blake, and H. J. Shaw, J. Lightwave Technol. **6**, 428 (1988).

[107]P. S. J. Russell, D. Culverhouse, and F. Farahi, Electron. Lett. **26**, 1195 (1990).

[108]G. Bahl, J. Zehnpfennig, M. Tomes, and T. Carmon, Nat. Commun. **2**, 403 (2011).

[109]E. A. Kittlaus, H. Shin, and P. T. Rakich, Nat. Photonics **10**, 463 (2016).

[110]P. Kornreich, H. Callen, and A. Gundjian, Phys. Rev. **161**, 815 (1967).

[111]E. Peral and A. Yariv, IEEE J. Quantum Electron. **35**, 1185 (1999).

[112]M. Tomes, F. Marquardt, G. Bahl, and T. Carmon, Phys. Rev. A **84**, 063806 (2011).

[113]J. E. Sipe and M. J. Steel, New J. Phys. **18**, 045004 (2016).

[114]P. Kharel, R. O. Behunin, W. H. Renninger, and P. T. Rakich, Phys. Rev. A **93**, 063806 (2016).

[115]C. Wolff, R. V. Laer, M. J. Steel, B. J. Eggleton, and C. G. Poulton, New J. Phys. **18**, 025006 (2016).

[116]P. Rakich and F. Marquardt, New J. Phys. **20**, 045005 (2018).

[117]A. B. Matsko, V. S. Ilchenko, A. A. Savchenkov, and L. Maleki, Phys. Rev. A **66**, 043814 (2002).

[118]Y. K. Chembo and C. R. Menyuk, Phys. Rev. A **87**, 053852 (2013).

[119]L. A. Lugiato and R. Lefever, Phys. Rev. Lett. **58**, 2209 (1987).

[120]G. P. Agrawal, *Nonlinear Fiber Optics* (Elsevier, 2013), pp. 129–191.

[121]M. Merklein, I. V. Kabakova, T. F. S. Buttner, D. Y. Choi, B. Luther-Davies, S. J. Madden, and B. J. Eggleton, Nat. Commun. **6**, 6396 (2015).

[122]J.-C. Beugnot and V. Laude, Phys. Rev. B **86**, 224304 (2012).

[123]X. Huang and S. Fan, J. Lightwave Technol. **29**, 2267 (2011).

[124]E. A. Kittlaus, N. T. Otterstrom, P. Kharel, S. Gertler, and P. T. Rakich, Nat. Photonics **12**, 613 (2018).

[125]B. C. P. Sturmberg, K. B. Dossou, M. J. A. Smith, B. Morrison, C. G. Poulton, and M. J. Steel, e-print arXiv:1811.10219v1 (2018).

[126]I. S. Grudinin, A. B. Matsko, and L. Maleki, Phys. Rev. Lett. **102**, 043902 (2009).

[127]I. S. Grudinin, H. Lee, O. J. Painter, and K. J. Vahala, Phys. Rev. Lett. **104**, 083901 (2010).

[128]K. Che, P. Zhang, C. Guo, D. Tang, C. Ren, H. Xu, Z. Luo, and Z. Cai, Opt. Commun. **387**, 421 (2017).

[129]K. J. Vahala, Phys. Rev. A **78**, 023832 (2008).

[130]A. L. Schawlow and C. H. Townes, Phys. Rev. **112**, 1940 (1958).

[131]M. Lax, Phys. Rev. **160**, 290 (1967).

[132]C. Montes, A. Mamhoud, and E. Picholle, Phys. Rev. A **49**, 1344 (1994).

[133]C. Metzger, M. Ludwig, C. Neuenhahn, A. Ortlieb, I. Favero, K. Karrai, and F. Marquardt, Phys. Rev. Lett. **101**, 133903 (2008).

[134]B. S. Sheard, M. B. Gray, C. M. Mow-Lowry, D. E. McClelland, and S. E. Whitcomb, Phys. Rev. A **69**, 051801 (2004).

[135] M. Ludwig, B. Kubala, and F. Marquardt, New J. Phys. **10**, 095013 (2008).

[136] A. Schliesser, R. Rivière, G. Anetsberger, O. Arcizet, and T. J. Kippenberg, Nat. Phys. **4**, 415 (2008).

[137] G. Bahl, M. Tomes, F. Marquardt, and T. Carmon, Nat. Phys. **8**, 203 (2012).

[138] S. Kim and G. Bahl, Opt. Express **25**, 776 (2017).

[139] S. Weis, R. Riviere, S. Deleglise, E. Gavartin, O. Arcizet, A. Schliesser, and T. J. Kippenberg, Science **330**, 1520 (2010).

[140] A. H. Safavi-Naeini, T. P. M. Alegre, J. Chan, M. Eichenfield, M. Winger, Q. Lin, J. T. Hill, D. E. Chang, and O. J. Painter, Nature **472**, 69 (2011).

[141] J. Kim, M. C. Kuzyk, K. Han, H. Wang, and G. Bahl, Nat. Phys. **11**, 275 (2015).

[142] C.-H. Dong, Z. Shen, C.-L. Zou, Y.-L. Zhang, W. Fu, and G.-C. Guo, Nat. Commun. **6**, 6193 (2015).

[143] C. Wolff, R. Soref, C. G. Poulton, and B. J. Eggleton, Opt. Express **22**, 30735 (2014).

[144] C. W. Barnes, Proc. IEEE **52**, 64 (1964).

[145] J. M. Manley and H. E. Rowe, Proc. IRE **44**, 904 (1956).

[146] D. F. Nelson and M. Lax, Phys. Rev. Lett. **24**, 379 (1970).

[147] A. Bichler, S. Lecler, B. Serio, S. Fischer, and P. Pfeiffer, J. Opt. Soc. Am. A **29**, 2386 (2012).

[148] A. W. Snyder and J. D. Love, *Optical Waveguide Theory* (Springer US, Boston, MA, 1984).

[149] B. A. Auld, *Acoustic Fields and Waves in Solids*, 2nd ed. (Wiley, 1992).

[150] R. A. Waldron, IEEE Trans. Microwave Theory Tech. **17**, 893 (1969).

[151] R. N. Thurston, J. Acoust. Soc. Am. **64**, 1 (1978).

[152] T. A. Birks, Y. W. Li, R. P. Kenny, and K. P. Oakley, Proc. Sixth Eur. Conf. Math. Ind. **8**, 319 (1992).

[153] P. F. Jarschel, L. S. Magalhaes, I. Aldaya, O. Florez, and P. Dainese, Opt. Lett. **43**, 995 (2018).

[154] M. S. Kang, A. Brenn, G. S. Wiederhecker, and P. S. J. Russell, Appl. Phys. Lett. **93**, 131110 (2008).

[155] A. Godet, A. Ndao, T. Sylvestre, V. Pecheur, S. Lebrun, G. Pauliat, J.-C. Beugnot, and K. Phan Huy, Optica **4**, 1232 (2017).

[156] D. S. Han, I.-M. Lee, K. H. Park, and M. S. Kang, Appl. Phys. Lett. **113**, 121108 (2018).

[157] H. E. Engan, J. Opt. Soc. Am. A **13**, 112 (1996).

[158] K. J. Lee, I.-K. Hwang, H. C. Park, and B. Y. Kim, Opt. Express **18**, 12059 (2010).

[159] J. Ko, K. J. Lee, and B. Y. Kim, Appl. Opt. **53**, 8499 (2014).

[160] C. Wolff, M. J. Steel, and C. G. Poulton, Opt. Express **22**, 32489 (2014).

[161] M. A. Yavorsky, D. V. Vikulin, E. V. Barshak, B. P. Lapin, and C. N. Alexeyev, Opt. Lett. **44**, 598 (2019).

[162] A. N. Oraevsky, Quantum Electron. **32**, 377 (2002).

[163] T. J. Kippenberg, H. Rokhsari, T. Carmon, A. Scherer, and K. J. Vahala, Phys. Rev. Lett. **95**, 033901 (2005).

[164] A. B. Matsko, A. A. Savchenkov, V. S. Ilchenko, D. Seidel, and L. Maleki, Phys. Rev. Lett. **103**, 257403 (2009).

[165] B. Sturman and I. Breunig, New J. Phys. **17**, 125006 (2015).

[166] S.-I. Tamura, Phys. Rev. B **79**, 054302 (2009).

[167] A. V. Dmitriev, D. S. Gritsenko, and V. P. Mitrofanov, Ultrasonics **54**, 905 (2014).

[168] K. J. Vahala, Nature **424**, 839 (2003).

[169] M. J. A. Smith, C. M. de Sterke, C. Wolff, M. Lapine, and C. G. Poulton, Phys. Rev. B **96**, 064114 (2017).

[170] M. J. A. Smith, B. T. Kuhlmey, C. M. de Sterke, C. Wolff, M. Lapine, and C. G. Poulton, Phys. Rev. B **91**, 214102 (2015).

[171] M. J. A. Smith, C. Wolff, C. G. Poulton, and C. Martijn de Sterke, Opt. Lett. **44**, 1407 (2019).

[172] M. Zhang, C. Wang, Y. Hu, A. Shams-Ansari, T. Ren, S. Fan, and M. Lončar, Nat. Photonics **13**, 36 (2018).

[173] B. Desiatov, A. Shams-Ansari, M. Zhang, C. Wang, and M. Lončar, Optica **6**, 380 (2019).

[174] M. Zhang, C. Wang, R. Cheng, A. Shams-Ansari, and M. Lončar, Optica **4**, 1536 (2017).

[175] C. Wang, M. Zhang, B. Stern, M. Lipson, and M. Lončar, Opt. Express **26**, 1547 (2018).

[176] C.-L. Zou, X. Han, L. Jiang, and H. X. Tang, Phys. Rev. A **94**, 013812 (2016).

[177] L. Fan, C.-L. Zou, M. Poot, R. Cheng, X. Guo, X. Han, and H. X. Tang, Nat. Photonics **10**, 766 (2016).

[178] C. Xiong, W. H. P. Pernice, X. Sun, C. Schuck, K. Y. Fong, and H. X. Tang, New J. Phys. **14**, 095014 (2012).

[179] M. J. Burek, J. D. Cohen, S. M. Meenehan, N. El-Sawah, C. Chia, T. Ruelle, S. Meesala, J. Rochman, H. A. Atikian, M. Markham, D. J. Twitchen, M. D. Lukin, O. J. Painter, and M. Lončar, Optica **3**, 1404 (2016).

[180] M. Mitchell, B. Khanaliloo, D. P. Lake, T. Masuda, J. P. Hadden, and P. E. Barclay, Optica **3**, 963 (2016).

[181] K. C. Balram, M. I. Davanço, J. D. Song, and K. Srinivasan, Nat. Photonics **10**, 346 (2016).

[182] H. Pfeifer, T. Paraïso, L. Zang, and O. J. Painter, Opt. Express **24**, 11407 (2016).

[183] X. Han, C.-L. Zou, and H. X. Tang, Phys. Rev. Lett. **117**, 123603 (2016).

[184] W. Jiang, R. N. Patel, F. M. Mayor, T. P. McKenna, P. Arrangoiz-Arriola, C. J. Sarabalis, J. D. Witmer, R. Van Laer, and A. H. Safavi-Naeini, e-print arXiv:1903.00957 [physics.optics] (2019).

[185] C. Wolff, P. Gutsche, M. J. Steel, B. J. Eggleton, and C. G. Poulton, Opt. Express **23**, 26628 (2015).

[186] S. R. Mirnaziry, C. Wolff, M. J. Steel, B. Morrison, B. J. Eggleton, and C. G. Poulton, Opt. Express **25**, 23619 (2017).

[187] D. Navarro-Urrios, N. E. Capuj, J. Gomis-Bresco, F. Alzina, A. Pitanti, A. Griol, A. Martínez, and C. M. Sotomayor Torres, Sci. Rep. **5**, 15733 (2015).

[188] I. Aldaya, A. Gil-Molina, J. L. Pita, L. H. Gabrielli, H. L. Fragnito, and P. Dainese, Optica **4**, 1219 (2017).

[189] R. Benevides, F. G. S. Santos, G. O. Luiz, G. S. Wiederhecker, and T. P. M. Alegre, Sci. Rep. **7**, 2491 (2017).

[190] V. Laude, *Phononic Crystals: Artificial Crystals for Sonic, Acoustic, and Elastic Waves*, De Gruyter Studies in Mathematical Physics (De Gruyter, 2015).

[191] S. D. Huber, Nat. Phys. **12**, 621 (2016).

[192] P. Wang, L. Lu, and K. Bertoldi, Phys. Rev. Lett. **115**, 104302 (2015).

[193] Y. Jin, D. Torrent, and B. Djafari-Rouhani, Phys. Rev. B **98**, 054307 (2018).

[194] G. Enzian, M. Szczykulska, J. Silver, L. Del Bino, S. Zhang, I. A. Walmsley, P. Del'Haye, and M. R. Vanner, Optica **6**, 7 (2019).

[195] W. H. Renninger, P. Kharel, R. O. Behunin, and P. T. Rakich, Nat. Phys. **14**, 601 (2018).

[196] A. H. Ghadimi, S. A. Fedorov, N. J. Engelsen, M. J. Bereyhi, R. Schilling, D. J. Wilson, and T. J. Kippenberg, Science **360**, 764 (2018).

[197] R. A. Norte, J. P. Moura, and S. Gröblacher, Phys. Rev. Lett. **116**, 147202 (2016).

[198] A. Butsch, M. S. Kang, T. G. Euser, J. R. Koehler, S. Rammler, R. Keding, and P. S. Russell, Phys. Rev. Lett. **109**, 183904 (2012).

[199] H. Seok, L. F. Buchmann, E. M. Wright, and P. Meystre, Phys. Rev. A **88**, 063850 (2013).

[200] P. Kharel, Y. Chu, E. A. Kittlaus, N. T. Otterstrom, S. Gertler, and P. T. Rakich, e-print arXiv:1812.06202 [physics.optics] (2018).

[201] L. Fan, K. Y. Fong, M. Poot, and H. X. Tang, Nat. Commun. **6**, 5850 (2015).

[202] W. H. P. Nielsen, Y. Tsaturyan, C. B. Møller, E. S. Polzik, and A. Schliesser, Proc. Natl. Acad. Sci. U. S. A. **114**, 62 (2017).

[203] E. A. Kittlaus, N. T. Otterstrom, and P. T. Rakich, Nat. Commun. **8**, 15819 (2017).

[204] N. T. Otterstrom, R. O. Behunin, E. A. Kittlaus, and P. T. Rakich, Phys. Rev. X **8**, 041034 (2018).

[205] K. E. Grutter, M. I. Davanço, and K. Srinivasan, Optica **2**, 994 (2015).

[206] R. N. C. Pfeifer, T. A. Nieminen, N. R. Heckenberg, and H. Rubinsztein-Dunlop, Rev. Mod. Phys. **79**, 1197 (2007).

[207] S. M. Barnett and R. Loudon, Philos. Trans. R. Soc., A **368**, 927 (2010).

[208] I. Brevik, Ann. Phys. **377**, 10 (2017).

[209] R. Loudon, S. M. Barnett, and C. Baxter, Phys. Rev. A **71**, 063802 (2005).

[210] B. A. Kemp, J. Appl. Phys. **109**, 111101 (2011).

[211] S. M. Barnett, Phys. Rev. Lett. **104**, 070401 (2010).

[212] A. Kundu, R. Rani, and K. S. Hazra, Sci. Rep. **7**, 42538 (2017).

[213] I. Brevik, Phys. Rev. A **98**, 043847 (2018).

[214] T. Požar, J. Laloš, A. Babnik, R. Petkovšek, M. Bethune-Waddell, K. J. Chau, G. V. B. Lukasievicz, and N. G. C. Astrath, Nat. Commun. **9**, 3340 (2018).

[215] T. J. Kippenberg and K. J. Vahala, Science **321**, 1172 (2008).

[216] T. J. Kippenberg and K. J. Vahala, Opt. Express **15**, 17172 (2007).

[217] C. Baker, W. Hease, D.-T. Nguyen, A. Andronico, S. Ducci, G. Leo, and I. Favero, Opt. Express **22**, 14072 (2014).

[218] V. Liu, M. Povinelli, and S. Fan, Opt. Express **17**, 21897 (2009).

[219] M. L. Povinelli, S. G. Johnson, M. Lončar, M. Ibanescu, E. J. Smythe, F. Capasso, and J. D. Joannopoulos, Opt. Express **13**, 8286 (2005).

[220] P. T. Rakich, M. Popović, M. Soljacic, and E. P. Ippen, Nat. Photonics **1**, 658 (2007).

[221] J. R. Rodrigues and V. R. Almeida, Opt. Lett. **42**, 4371 (2017).

[222] D. F. Nelson, Phys. Rev. A **44**, 3985 (1991).

[223] R. Van Laer, e-print arXiv:1605.09645 (2016).

[224] B. A. Kemp and E. Wolf, *Progress in Optics* (Elsevier, 2015), pp. 437–488.

[225] M. Mansuripur, Appl. Phys. A: Mater. Sci. Process. **123**, 653 (2017).

[226] C. J. Sarabalis, J. T. Hill, and A. H. Safavi-Naeini, APL Photonics **1**, 071301 (2016).

[227] M. A. Hopcroft, W. D. Nix, and T. W. Kenny, J. Microelectromech. Syst. **19**, 229 (2010).

[228] D. K. Biegelsen, Phys. Rev. Lett. **33**, 51 (1974).

[229] G. O. Luiz, R. S. Benevides, F. G. S. Santos, Y. A. V. Espinel, T. P. Mayer Alegre, and G. S. Wiederhecker, Opt. Express **25**, 31347 (2017).